Active Reconfigurable Intelligent Surface Architectures for Future Wireless Networks

by

Recep Akif TAŞÇI

A Dissertation Submitted to the
Graduate School of Sciences and Engineering
in Partial Fulfillment of the Requirements for
the Degree of

Master of Science

in

Electrical and Electronics Engineering

KOÇ ÜNİVERSİTESİ

September 1, 2022

Active Reconfigurable Intelligent Surface Architectures for Future Wireless Networks

Koç University

Graduate School of Sciences and Engineering

This is to certify that I have examined this copy of a master's thesis by

Recep Akif TAŞÇI

and have found that it is complete and satisfactory in all respects,
and that any and all revisions required by the final
examining committee have been made.

Committee Members:

_____

Assoc. Prof. Ertuğrul BAŞAR (Advisor)

_____

Prof. Sinem ÇÖLERİ

_____

Assoc. Prof. Mehmet Kemal ÖZDEMİR

Date: _____

I dedicate this thesis to my dear family.

ABSTRACT

Active Reconfigurable Intelligent Surface Architectures for Future Wireless Networks
Recep Akif TAŞÇI
Master of Science in Electrical and Electronics Engineering
September 1, 2022

Reconfigurable intelligent surface (RIS)-assisted communication has recently attracted the attention of the wireless communication community as a potential candidate for 6th generation (6G) of wireless networks. Various studies have been carried out on the RIS technology, which is capable of enabling the control of the signal propagation environment by network operators. However, when an RIS is used in its inherently passive structure, it appears to be only a supportive technology for communications, while suffering from a multiplicative path loss. Therefore, researchers have lately begun to focus on RIS hardware designs with minimal active elements to further boost the benefits of this technology. In this thesis, first, we present a simple RIS hardware architecture including a single and variable gain amplifier for reflection amplification to confront the multiplicative path loss. The end-to-end signal model for communication systems assisted with the proposed amplifying RIS design is presented, together with an analysis focusing on the capacity maximization and theoretical bit error probability performance, which is corroborated by computer simulations. In addition, the major advantages of the proposed amplifying RIS design compared to its passive counterpart are discussed. It is shown that the proposed RIS-based wireless system significantly eliminates the double fading problem appearing in conventional passive RIS-assisted systems and improves the communication energy efficiency.

This thesis also introduces an RIS-assisted grant-free non-orthogonal multiple access (GF-NOMA) scheme. We propose a joint user equipment (UE) clustering and RIS assignment/alignment approach that ensures the power reception disparity required by the power domain NOMA (PD-NOMA). The proposed approach maximizes the network sum rate by judiciously pairing UE with distinct channel gains and assigning RISs to proper clusters. To alleviate the computational complexity

of the joint approach, we decouple UE clustering and RIS assignment/alignment subproblems, which reduces run times 80 times while attaining almost the same performance. Once the proposed approaches acknowledge UEs with the cluster index, UEs are allowed to access corresponding resource blocks (RBs) at any time requiring neither further grant acquisitions from the base station (BS) nor power control as all UEs are requested to transmit at the same power. In addition to passive RISs containing only passive elements and giving an 18% better performance, a fully-connected active RIS structure that enhances the performance by 37% is also used to overcome the double path loss problem. The numerical results also investigate the impact of UE density, RIS deployment, RIS hardware specifications, and the fairness among the UEs in terms of bit-per-joule energy efficiency.

ÖZETÇE

Yüksek Lisans Tez Başlığı
Recep Akif TAŞÇI
Elektrik ve Elektronik Mühendisliği, Yüksek Lisans
1 Eylül 2022

Yeniden yapılandırılabilir akıllı yüzey (RIS) destekli haberleşme, gelecek 6'ıncı nesil (6G) kablosuz ağlar için potansiyel bir aday olarak kablosuz haberleşme topluluğunun yakın zamanda dikkatini çekmiştir. Sinyal yayılım ortamının şebeke operatörleri tarafından kontrol edilmesini sağlayan RIS teknolojisi üzerinde çeşitli çalışmalar yapılmıştır. Bununla birlikte, bir RIS doğası gereği pasif yapısında kullanıldığında çarpımsal bir yol kaybından muzdarip olduğundan, haberleşme sistemleri için yalnızca destekleyici bir teknoloji gibi görünmektedir. Bu nedenle, araştırmacılar son zamanlarda bu teknolojinin faydalarını daha da artırmak için minimum aktif elemanlı RIS tasarımlarına odaklanmaya başlamışlardır. Bu çalışmada, çarpımsal yol kaybını tolere etmek amacıyla değişken kazançlı tek bir yükselteç içeren basit bir RIS mimarisi sunuyoruz. Önerilen bu yükseltici RIS tasarımı ile desteklenen bir haberleşme sistemi için uçtan uca sinyal modeli ve kanal kapasitesi maksimizasyonu sunulmuştur. Bununla beraber teorik bit hata olasılığı performansına odaklanan bir analiz ile birlikte kanal kapasitesi sunulmaktadır. Ek olarak, önerilen yükseltici RIS tasarımının pasif versiyonu ile karşılaştırıldığında başlıca avantajları tartışılmıştır. Önerilen RIS tabanlı kablosuz haberleşme sisteminin, sıradan pasif RIS destekli sistemlerde ortaya çıkan çift sönümleme sorununu önemli ölçüde ortadan kaldırdığı ve enerji verimliliğini iyileştirdiği gösterilmiştir.

Bu tez aynı zamanda bir RIS destekli hibesiz dikgen olmayan çoklu erişim (GF-NOMA) şemasını tanıtmaktadır. Güç eksenli NOMA'nın (PD-NOMA) gerektirdiği güç dağılımı farklılığını sağlayan birleşik bir kullanıcı ekipmanı (UE) kümele- me ve RIS atama algoritması önerilmiştir. Bu yaklaşım, UE'yi farklı kanal kazançları ile akıllıca eşleştirerek ve RIS'leri uygun kümelere atayarak ağ kapasitesini maksimuma çıkarır. Bu birleşik algoritmanın hesaplama karmaşıklığını hafifletmek için, performanstan ödün vermeden algoritmanın çalışma süresini 80 kat azaltan başka bir UE kümeleme ve RIS atama algoritması geliştirilmiştir. Önerilen yaklaşımlar

küme indeksi ile UE'leri onayladıktan sonra, tüm UE'lerin aynı anda iletmeleri istendiğinden, UE'lerin herhangi bir zamanda ne baz istasyonundan (BS) daha fazla hibe edinimi ne de güç kontrolü gerektirmeyen ilgili kaynak bloklarına (RBs) erişmesine izin verilir. Sadece pasif elemanlar içeren ve %18 daha iyi performans veren pasif RIS'lere ek olarak, çift yol kayıp problemini aşmak için performansı %37 arttıran tam bağlantılı aktif RIS yapısı da kullanılmaktadır. Ayrıca, elde edilen sonuçlar UE yoğunluğun, RIS konuşlandırılmasının ve RIS donanım spesifikasyonlarının etkilerini, ve Joule başına bit enerji verimliliği açısından UE'ler arasındaki güç harcama adilliğini ortaya koyar.

ACKNOWLEDGMENTS

I would like to thank my mentors, Assoc. Prof. Ertuğrul BAŞAR and Assoc. Prof. Mehmet Kemal ÖZDEMİR, who have always enlightened me with valuable knowledge and advice, with my genuine gratitude and warm regards. I am grateful that they made me feel their trust and kind support. I feel fortunate to have the opportunity to work with them.

I would like to express my gratitude with my deepest love to my beloved parents, Muammer and Nermin TAŞÇI, who have always supported me. No matter what, they made me know right from wrong and always trusted in me to find the correct path. I would also like to thank my sisters and brothers, Şükran, Melek, Emine, Mustafa Yasin and Ali Osman TAŞÇI, for their support. They were always on my side and never left me down.

I would also like to thank my close friend Fatih KILINÇ, with whom I have always worked. We have shared not only every information we learned but everything we had. He was always like a brother to me and always will be.

Last but not least, I also wish to thank my beloved one, İrem Tuba ARSLAN, for her endless love. She encourage and support me everytime when I fall into despair. She is the most beautiful thing I have found in this world.

TABLE OF CONTENTS

List of Tables **xi**

List of Figures **xii**

Abbreviations **xiv**

Chapter 1: Introduction **1**

1.1 Main Contributions 6

1.2 Notations and Organization 8

Chapter 2: Reconfigurable Intelligent Surfaces and NOMA Networks **10**

2.1 Passive RISs 10

2.2 Active RISs 11

2.3 RIS-Assisted NOMA Networks 12

2.4 GF-NOMA Networks 13

Chapter 3: A New RIS Architecture with a Single Power Amplifier: Energy Efficiency and Error Performance Analysis **15**

3.1 System Model 15

3.1.1 Amplifying RIS-assisted System 15

3.1.2 Passive RIS-assisted System 19

3.2 Performance Analysis 20

3.3 Total Power Consumption Model and Energy Efficiency Analysis . . . 23

3.4 Numerical Results 25

3.4.1 Performance Evaluation 26

3.4.2 Energy Efficiency Evaluation 31

Chapter 4: RIS-Assisted Grant-Free NOMA: User Pairing, RIS Assignment, and Phase Shift Alignment **35**

4.1 System Model 35

4.1.1 Network Model 35

4.1.2 Channel Model 37

4.1.3 Passive RIS-Assisted NOMA System 38

4.1.4 Active RIS-Assisted NOMA System 39

4.2 Problem Definition and Solution Methodology 42

4.2.1 Problem Definition 42

4.2.2 Solution Methodology 43

4.3 UE Clustering and RIS Assignment Algorithms 44

4.3.1 Joint 3D UE Clustering and RIS Assignment Algorithm . . . 44

4.3.2 Consecutive 2D UE Clustering and RIS Assignment Algorithm 47

4.4 Numerical Results 50

4.4.1 Benchmark Schemes 50

4.4.2 Impact of UE Density on Sumrate and Time Complexity . . . 52

4.4.3 The Impact of Identical Tx Power on Fairness 53

Chapter 5: Conclusion **57**

Bibliography **59**

Appendix A: **69**

LIST OF TABLES

1.1 Comparison of the proposed architecture with a passive RIS, a fully-connected active RIS, and a multi-antenna AF relay 4

3.1 Power consumption model parameters 25

4.1 Table of the simulation parameters 51

A.1 The shape (k) and scale (ν) parameters of the fitted Gamma distribution 70

LIST OF FIGURES

1.1 Proposed Active RIS Architecture 3
1.2 Illustration of the RIS-aided GF-NOMA networks 6

2.1 Passive RIS [Zhang *et al.*, 2021] 10
2.2 Active RIS [Zhang *et al.*, 2021] 11

3.1 Generic system model for the considered amplifying RIS-assisted scheme. 16
3.2 Generic system model for a passive RIS-assisted scheme. 19
3.3 The PDF of γ_{act} and Gamma distribution fits for (a) $N = 10, \ldots, 20$ and (b) $N = 300, \ldots, 400$. 22
3.4 BER results for (a) $P_{\max} = 10$ dBm and (b) $P_{\max} = 20$ dBm. 26
3.5 Achievable rates of the system for (a) $d_h = 50$ m and (b) $d_h = 100$ m. 27
3.6 Achievable rates of the amplifying RIS-assisted system for (a) $P_t = 20$ dBm and (b) $P_t = 10$ dBm. The numbers on the markers indicate G_{opt} values. 29
3.7 Achievable rates of the amplifying RIS-assisted system for different P_t and $P_{\max}$. 30
3.8 (a) Energy efficiencies of the amplifying RIS-assisted system for varying N and (b) corresponding achievable rates and P_{tot} values 31
3.9 (a) Energy efficiencies for different $P_{\max}$ values varying with P_t and (b) corresponding achievable rates and P_{tot} values 32
3.10 (a) Energy efficiencies for different P_t values varying with $P_{\max}$ and (b) corresponding achievable rates and P_{tot} values 33

4.1 Outer and inner cells of the network 36

4.2 (a) Sum rate and complexity of the proposed algorithms, and (b) sum rate of the proposed schemes 52
4.3 Sum rate and Jain's fairness index for varying p_{id} for the proposed and benchmark schemes 53
4.4 Sum rate of the network for different varying RIS metrics: (a) $\boldsymbol{D}_{\text{out}}$ and (b)$\boldsymbol{R}$. 55
4.5 Sum rate of the network for different varying N. 56

ABBREVIATIONS

AA	Axial Assignment
AF	Amplify-and-Forward
BEP	Bit Error Probability
BER	Bit Error Rate
BPSK	Binary Phase-Shift Keying
BS	Base Station
CLT	Central Limit Theorem
CSI	Channel State Information
DF	Decode-and-Forward
DMA	Dynamic Metasurface Antenna
EE	Energy Efficiency
GB	Grant-Based
GF	Grant-Free
LNA	Low-Noise Amplifier
LoS	Line-of-Sight
MGF-NOMA	Multi-Level Grant-Free non-Orthogonal Multiple Access
MIMO	Multiple-Input Multiple-Output
MINLP	Mixed-Integer non-Linear Programming
mMTC	Massive Machine-type Communications
MRC	Maximum Ratio Combining
NLoS	Non-Line-of-Sight
NOMA	Non-orthogonal Multiple Access
NP	Non-Deterministic Polynomial-Time
OMA	Orthogonal Multiple Access

OPT PD-NOMA	Optimum Power-Domain non-Orthogonal Multiple Access
PA	Power Amplifier
PD	Power Domain
PLS	Physical Layer Security
PSK	M-ary Phase-Shift Keying
PUCSH	Physical Uplink Shared Channel
PUCCH	Physical Uplink Control Channel
RB	Resource Block
RF	Radio Frequency
RIS	Reconfigurable Intelligent Surface
Rx	Receiver
SE	Spectral Efficiency
SEP	Symbol Error Probability
SGF-NOMA	Single Level Grant Free non-Orthogonal Multiple Access
SIC	Successive Interference Cancellation
SINR	Signal-to-Noise-Plus-Interference-Ratio
SISO	Single-Input Single-Output
SNR	Signal-to-Noise Ratio
SRS	Sounding Reference Signals
STAR	Simultaneously Transmitting and Receiving
TDD	Time-Division Duplexing
Tx	Transmitter
UE	User Equipment
UL	Uplink
UMa	Urban Macro
UpPTS	Uplink Pilot Time Slot
3D	Three-Dimensional
6G	6th Generation

Chapter 1

INTRODUCTION

The number of mobile users trying to keep up with emerging technologies is increasing day by day. This situation has an impact on many things around the world, especially on communication networks. Recent generations of wireless communication have been developed to meet the high data demand arising from these technological developments [Saad et al., 2020]. For these reasons, the fact that existing communication systems will start to become insufficient in the future, as it was before, will make the development of next generation of the wireless communication, 6th generation (6G) and beyond, inevitable. 6G focuses further enhancing data rate, security, consistency, and mobility, compared to its predecessors. In order to meet the future demands, numerous studies are being carried out towards 6G wireless networks. As a result, the use of advanced technologies such as extreme multiple-input multiple-output (MIMO) systems with power efficient front-ends [Shlezinger et al., 2021], as well as Terahertz and millimeter-wave communications might play an important role in supplying these demands.

In recent years, reconfigurable intelligent surface (RIS)-empowered communication has become one of the most popular developments towards 6G networks [Basar et al., 2019, Huang et al., 2019, Calvanese Strinati et al., 2021a, Di Renzo *et al.*, 2019, Wu et al., 2021, Calvanese Strinati et al., 2021b, Jian et al., 2022]. Supporting high wireless channel capacity, expanding the signal coverage, reducing the bulkiness of the multiple antenna systems as well as the energy consumption, low-cost implementation and mitigating several negative effects of the wireless channel, such as multipath fading and the Doppler effect can be given as some of the main reasons why RISs has been investigated thoroughly [Yildirim et al., 2021b, Basar, 2021, Wu

and Zhang, 2020].

Numerous studies have been conducted by combining RISs with many other techniques. Assisting a relay system with an RIS [Yildirim et al., 2021a], RIS-based index modulation [Basar, 2020], RIS-enabled reflection modulation [Lin et al., 2021, Yuan et al., 2021], implementation of non-orthogonal multiple access (NOMA) by using RISs [Zuo et al., 2020, Khaleel and Basar, 2021], and channel modeling in the presence of an RIS [Basar and Yildirim, 2020, Basar et al., 2021, Kilinc et al., 2021] can be given as notable examples. These studies have succeeded with the help of RISs but have not been able to avoid the performance degradation caused by the double path loss problem when the RIS is not positioned close to terminals [Basar and Poor, 2021, Dunna et al., 2020]. Therefore, passive RISs cannot go beyond being a supportive technology for communication systems due to the double path loss problem. Some studies have been conducted to overcome the double path loss effect by combining active elements with RISs. In [Alexandropoulos and Vlachos, 2020], a single receive radio frequency (RF) chain that includes a low-noise amplifier (LNA) was used to enable baseband reception, which in turn, was exploited for channel estimation at the RIS side. Similarly, channel estimation using a hybrid RIS architecture has been performed in [Alexandropoulos et al., 2021] by deploying small numbers of receive RF chains at the RIS side. Another RIS-based channel sensing approach was studied in [Alamzadeh et al., 2021] by coupling some incident signals with a modified RIS architecture, including receive RF chains. Furthermore, [Shlezinger et al., 2021] analyzes dynamic metasurface antennas (DMAs) from an analog and digital signal processing perspective with less number of RF chains than the number of metamaterials. In [Zhang *et al.*, 2021], a reflection-type amplifier has been proposed to be used by each reflecting element of an RIS, and the proposed active RIS element was designed, fabricated, and experimental results are provided. Another active reflecting element design has been proposed in [Long et al., 2021] such that the magnitude of the reflection coefficient of the reflecting elements is greater than unity. Connecting only a few elements of an RIS with RF chains and power amplifiers (PAs) has been investigated in [Nguyen et al., 2021] as a hybrid relay-reflecting intelligent surface.

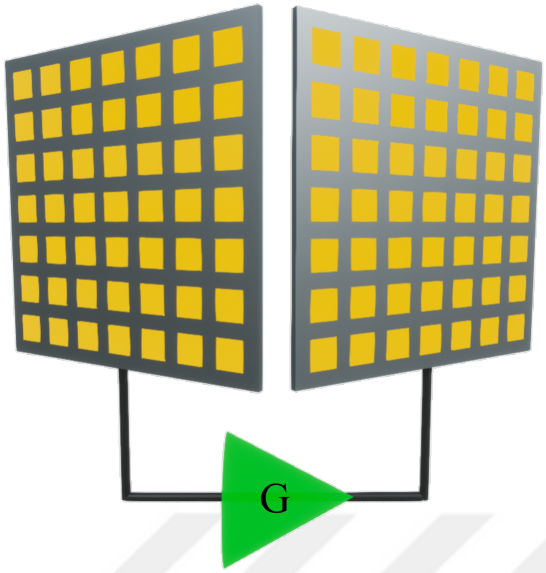

Figure 1.1: Proposed Active RIS Architecture

Against this background, as the first contribution, this thesis proposes an amplifying RIS design that incorporates a single PA and two RISs. According to our design, the signals received by elements of the first RIS are combined after getting their phase configured. Then, the combined signal is fed to the available PA, which feeds it to the second RIS that transmits it with a controllable phase configuration as shown in Fig. 1.1

The proposed design works solely in the RF domain, similar to the waveguide-based approach in [Alamzadeh et al., 2021], unlike full-duplex multi-antenna decode-and-forward (DF) relays, which perform down-conversion and baseband processing [Yildirim et al., 2021a]. Therefore, our design looks more similar to a full-duplex, multi-antenna, and amplify-and-forward (AF) relay. However, they have some key differences. Relays usually perform linear processing techniques, such as maximum ratio combining (MRC), and realize power allocation optimization algorithms. Furthermore, they include bulky phase-shifter networks for transmit beamforming and are subject to loopback self-interference [Uysal, 2009]. Our design is simpler, does not require complex algorithms, and prevents loopback self-interference via spatial separation in the form of back to back placement of the different RISs. Note that simple self-interference cancellation techniques in the RF domain can be applied

Table 1.1: Comparison of the proposed architecture with a passive RIS, a fully-connected active RIS, and a multi-antenna AF relay

	Proposed Design	**Passive RIS**	**Fully-Connected Active RIS**	**AF Relay**
Complexity	Low	Low	High	High
Power Consumption	Low	Low	High	High
Interference Cancellation	No interference	No interference	No interference	Signal processing required
Cost	Low	Low	High	High
Performance	High	Low	High	High

[Alexandropoulos et al., 2020].

A detailed comparison of the proposed scheme with passive RISs, fully-connected active RIS and AF relay is presented in Table 1.1. Considering fully-connected active designs, where each RIS element contains an active component, there are some drawbacks, such as power consumption and cost. These architectures may not be feasible for a large number of reflecting elements because they contain numerous active components. The proposed design has the key advantages of being energy efficient and low cost compared to other active RIS designs since it includes a single PA. Furthermore, the fully-connected active RIS architecture is more complex than the proposed system because the gain of each active element needs to be configured. In contrast, the gain of a single PA is adjusted in the proposed architecture. Although the fully-connected active RIS design is more powerful because of the amplifiers being connected to each reflecting element, the proposed scheme also benefits from the passive beamforming of the receiving and transmitting parts of the RIS. Compared to passive RISs, the proposed design enhances the system capacity in a more energy efficient manner. Moreover, as our system diminishes the effect of double path loss due to the amplification, it provides flexibility to place the RIS at any point between the transmitter (Tx) and the receiver (Rx). However, the pro-

posed design is more complex because additional signal processing procedures are required, such as adjusting the gain of the PA and phase configurations of the RISs.

We note that a similar concept was considered in [Abari et al., 2017], assuming that the received signal is amplified and fed back as leakage to the input; however, it lacks a sufficient mathematical framework and does not present detailed modeling of the system operation. On the other hand, in this thesis, we propose a novel amplifying RIS scheme with a solid mathematical framework and provide a unified model for the system operation. Moreover, we analyze the theoretical bit error probability (BEP), capacity, and energy efficiency (EE) of the proposed design and compare it with a benchmark passive RIS structure.

Moreover, NOMA has also been recognized as a promising candidate to enable enhanced massive machine-type communications (mMTC) by multiplexing several user equipments (UEs) on the same network resources [Saito et al., 2013, Islam et al., 2017]. In particular, power domain (PD)-NOMA improves the spectral efficiency (SE) by multiplexing UEs with different channel gain and transmit power such that successive interference cancellation (SIC) can be performed at the receiver. As the network size increases, PD-NOMA starts suffering from power control complexity, UE pairing and resource allocation overhead and ramifications of channel state information (CSI) acquisition [Shahab et al., 2020]. NOMA has also been investigated with emerging technologies such as index modulation [Arslan et al., 2020], cognitive radios [Arzykulov et al., 2021], and unmanned aerial vehicles-aided wireless networks [Arzykulov et al., 2022]. Recently, RISs have received attention thanks to their ability to create the reception power disparity required by PD-NOMA. While the RIS-aided NOMA is analyzed in [Hou et al., 2020a], dynamic and static RIS configurations for multi-user NOMA schemes are considered in [Liu et al., 2022]. The authors of [Khaleel and Basar, 2022] have studied partitioning of RIS to facilitate PD-NOMA. Noting that all of the mentioned schemes are grant-based (GB), there is still a dire need to address the signaling overhead and computational complexity issues. For this reason, research on grant-free NOMA (GF-NOMA) schemes that UEs can operate without grant acquisition recently received much attention. In particular, power-domain GF-NOMA schemes aim to eliminate the need for power

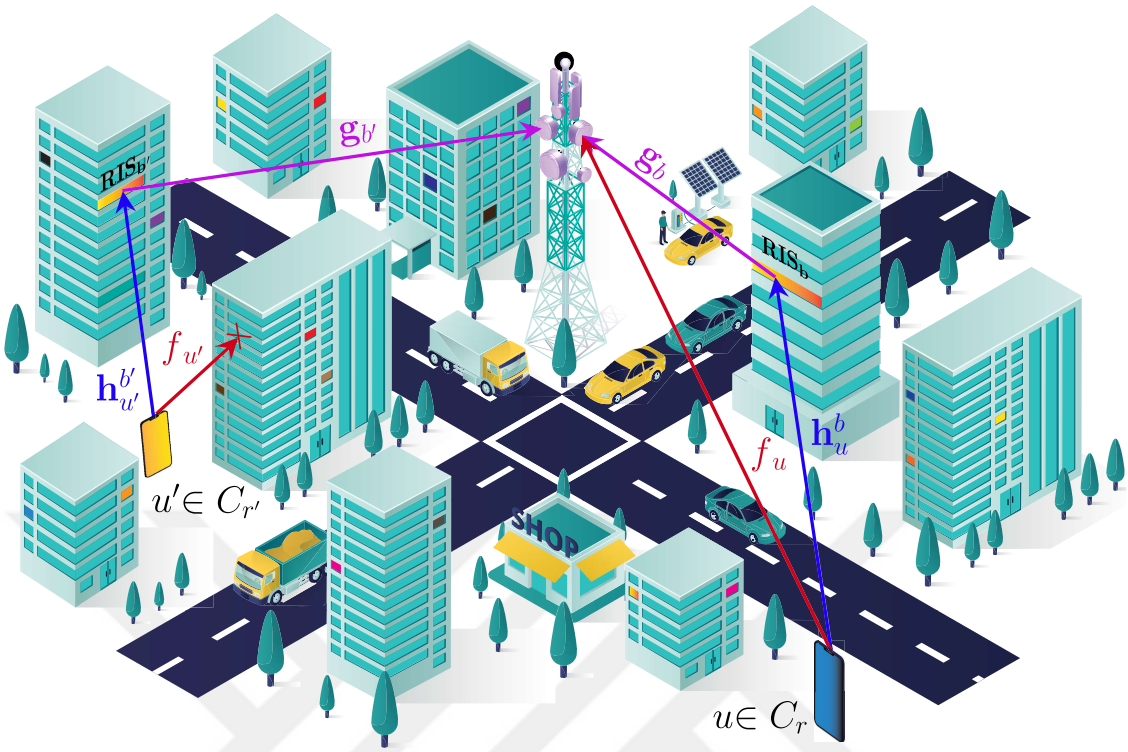

Figure 1.2: Illustration of the RIS-aided GF-NOMA networks

control and CSI acquisition at the transmitter side so that UEs can access allocated resource blocks (RBs) at any time without requiring grant acquisition. We have obvserved that the active RIS technology might be very promising for emerging NOMA systems as well. Therefore, in this thesis, we also decided to implement an RIS-aided GF-NOMA scheme where power reception disparity is ensured utilizing novel algorithms dealing with UE clustering, RIS assignment, and RIS phase shift alignment, considering a network consisting of a specific number of users and RISs distributed randomly over the cell coverage area as depicted in Fig. 1.2, where RIS blocks deployed on building facades/windows are highlighted in various colors.

1.1 Main Contributions

The main contributions of this thesis are summarized as follows:

- A new and energy efficient amplifying RIS design is proposed. The end-to-end system model of the proposed amplifying RIS design is presented.

- A cheaper, less complex, and more energy-efficient architecture than fully connected active RIS designs and multi-antenna AF relays is demonstrated.

- The proposed active RIS design provides the flexibility to position the RIS at any location, with an increase in performance compared to passive RISs.

- The achievable rate and the EE of the proposed amplifying RIS system are examined under different configurations, and an optimization problem is addressed to maximize the system capacity. Moreover, the theoretical BEP is obtained under different conditions, while being also verified through computer simulations.

- The proposed active RIS model is comprehensively compared with a passive RIS setup.

- This thesis also introduces an RIS-assisted fully GF-NOMA scheme where the required power disparity is obtained by three levels of implicit power control: clustering UEs with different channel gains into the same cluster, properly assigning RISs to UE clusters to increase power reception disparity, and aligning the phase shift matrix of RISs according to the cluster members to reach the highest possible network sum rate. In this way, the proposed approaches perform an over-the-air power control by judiciously pairing UEs, assigning RISs, and aligning phase shifts of RISs.

- Since optimizing UE clustering and RIS assignment/alignment for the maximum network sum rate is a non-deterministic polynomial-time (NP)-Hard problem, we propose two solution methodologies. In the former, we develop an iterative approach where each iteration exploits a three-dimensional axial assignment (3D-AA) problem for joint UE clustering, RIS assignment, and phase shift alignment. Since 3D cost matrix generation complexity increases with the number of UEs and RISs, the latter method decouples UE clustering and RIS assignment/alignment subproblems, which yields 80 times faster

completion time while reaching almost the same performance as the joint approach. The proposed schemes are designed to be applicable for both passive and active RIS architectures. The active RIS architecture considers a fully connected design where each element is connected to a PA, which introduces an extra power budget constraint on the optimization problem.

- The network-level simulations show that the proposed RIS-assisted GF-NOMA schemes outperform optimal GB PD-NOMA and regular GF-NOMA schemes. The active and passive RIS-assisted schemes provide %34 and %15 higher sum rate in a network where 150 UEs sharing 25 RBs, respectively. The network size simulation investigates the deployment scenarios, number of available RIS blocks and number of RIS elements. Deploying the RISs closer to the BS can yield up to %15 higher performance than a uniform distribution of the RISs across the cell area. The fairness among the UEs sharing the same RB is compared in terms of bit-per-joule energy efficiency by obtaining Jain's fairness index. While the proposed active RIS-assisted scheme provides the fairest scheme up to a 10 dB transmit power level, the passive RIS-assisted scheme achieves the same fairness as regular GF-NOMA schemes, and they both enhance the network capacity.

1.2 Notations and Organization

Throughout the thesis, sets and their cardinality are denoted with calligraphic and regular uppercase letters (e.g., $|\mathcal{A}| = A$), respectively. Vectors and matrices are represented in lowercase and uppercase boldfaces (e.g., $\mathbf{a}$ and $\mathbf{A}$), respectively. The i^{th} member of a vector and set is denoted by a_i and $\mathcal{A}\{i\}$, respectively. Likewise, matrix $\mathcal{A}$'s entry on i^{th} row and j^{th} column is denoted by $\mathcal{A}[i, j]$. Subscripts b, r and u are used for indexing the RIS blocks, RB/cluster, and UEs, respectively.

The rest of the thesis is organized as follows. In Chapter 2, a literature review about passive and active RISs, and GF-NOMA networks is presented. The system models and numerical results of a communication link assisted by the proposed RIS scheme, and a GF NOMA network assisted by fully-connected active RISs are

presented in Chapter 3 and Chapter 4, respectively. Finally, the thesis is concluded in Chapter 5.

Chapter 2

RECONFIGURABLE INTELLIGENT SURFACES AND NOMA NETWORKS

In this chapter, a brief description of passive and active RIS structures, and RIS-Assisted and Grant-Free NOMA networks is given.

2.1 Passive RISs

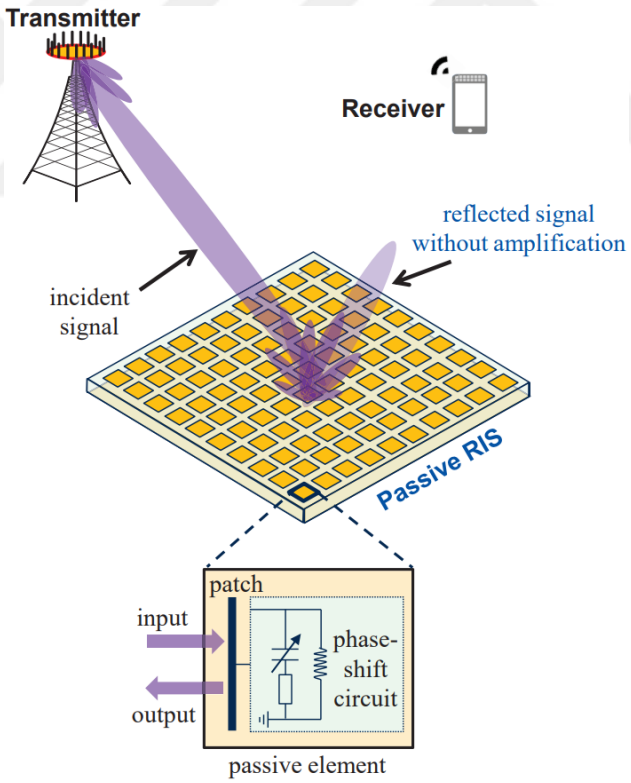

Figure 2.1: Passive RIS [Zhang *et al.*, 2021]

Massive antenna arrays include multiple RF chains attached to the antennas. Differently, RISs include only a certain number of reflecting elements that reflect the incoming signals with a specific phase as shown in Fig. 2.1. This operation can be

done by changing the electromagnetic properties of their reflecting elements, such as the reflection coefficient, with the help of a software-defined controller. In that way, the wireless propagation environment becomes configurable. The potential of RISs stems from the fact that they perform these operations while being almost passive because tiny reflecting elements are used instead of power-hungry phase shifters. Thus, energy efficient and low cost setups can be realized with the help of RISs.

2.2 Active RISs

Similar to passive RIS, active RISs reflect signals incoming to their elements by changing their phase. In addition, active RISs contain some active elements that amplify the incoming signals as shown in Fig. 2.2. Amplified and phase-optimized signals cause greater signal strength at the receiver. Thus, the signal-to-noise ratio (SNR) at the receiver reaches higher values. Although the use of active elements causes additional power consumption, it is often much more advantageous in terms of

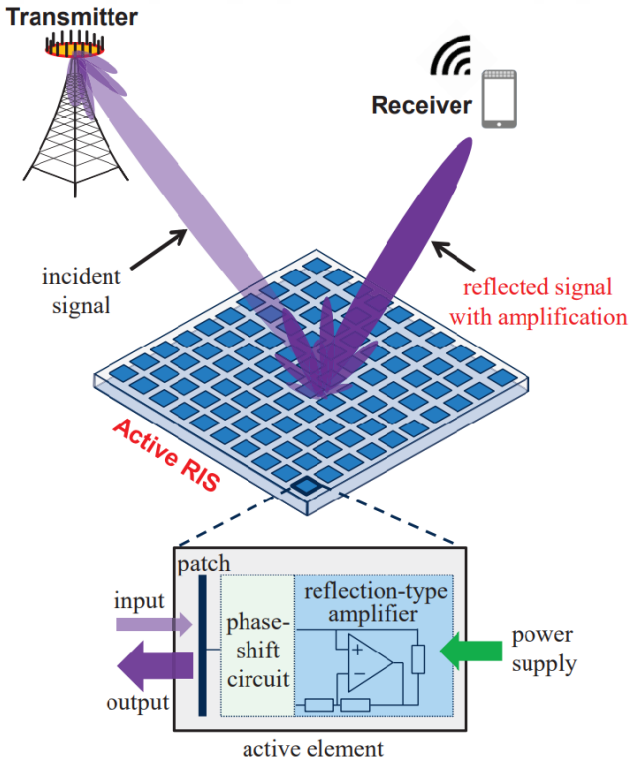

Figure 2.2: Active RIS [Zhang *et al.*, 2021]

energy efficiency as there is a significant increase in SNR at the receiver. In addition to these advantages of active RISs, the thermal noise produced by the active elements used can be seen as a disadvantage. The situation may seem even worse given the fact that the thermal noise will also be amplified by the active elements. But some setups can be realized where the amplified thermal noise is attenuated or neglected. As a result, active RISs can greatly improve communication systems in general, even if they have some disadvantages.

2.3 RIS-Assisted NOMA Networks

RISs have received attention thanks to their ability to create the reception power disparity required by PD-NOMA [C.Pan *et al.*, 2021]. The authors compare the RIS-assisted orthogonal multiple access (OMA) and NOMA technologies from different aspects and evaluate the performance of static and dynamic RISs in [Liu et al., 2022]. In [Hou et al., 2020b], the authors design passive beamforming weights to boost the performance of the PD-NOMA and propose a priority-oriented NOMA scheme to increase SE. In [Yang et al., 2021a], the authors aim to maximize the minimum signal-to-noise-plus-interference-ratio (SINR) threshold by deploying RISs in NOMA networks. Integration of the RIS technology to NOMA brings optimization problems such as joint optimal power allocation, RIS phase configuration, and UE allocation to obtain the best performance from the two technologies. To address these problems [Liu et al., 2021b] uses a two-step machine learning approach for joint deployment, phase shift design, and power allocation. Also, [Yang et al., 2021b] uses machine learning algorithms for UE partitioning and phase shifter network design. [Zhong et al., 2022] investigates the artificial intelligence empowered RIS-NOMA networks by using deep reinforcement learning. The existing literature also inspects RIS-NOMA schemes from the physical layer security perspective. In [Tang et al., 2021], authors propose novel RIS-assisted NOMA schemes for enhancing the physical layer security (PLS). The study in [Zhang et al., 2021] proposes sub-optimal joint beamforming and power allocation scheme to increase the PLS as well. The RISs are also used for serving cell-edge UEs by integrating RIS technology into joint

transmission-coordinated multipoint in a two-cell NOMA-based network in [Elhattab et al., 2021]. Using different RIS designs and partitioning RIS into sub-surfaces are also proposed to serve multiple UEs simultaneously to employ NOMA. The authors in [Khaleel and Basar, 2022] propose RIS partitioning to employ NOMA and maximize UE fairness. Furthermore, [Aldababsa et al., 2022, Aldababsa et al., 2021] use simultaneously transmitting and receiving (STAR) RIS in NOMA networks and evaluate from an error performance perspective. The hardware impairments of the RIS also considered in the literature, and the effects on the outage probability [Hemanth et al., 2020] and secrecy rate [Chen et al., 2021] is investigated.

2.4 GF-NOMA Networks

GF access appears to be a savior technology for NOMA networks. GB NOMA networks require the UEs in the same cluster to know the CSI of other members and align their transmission power accordingly. This process also causes a considerable signaling overhead and computational complexity on the UE side. Therefore scientists are looking for ways to exclude the computation on the UE side and enable them to access the base station (BS) without grant permission. Multiple access based, compute and forward-based, compressed sensing-based GF-NOMA schemes are presented, and future directions of GF-NOMA technology are given in [Shahab et al., 2020]. The ALOHA-NOMA schemes are proposed in [Balevi et al., 2018, Elkourdi et al., 2018] which provide high throughput and lower complexity. Semi-GF schemes where GB and GF UEs share the same spectrum are evaluated from the stochastic geometry perspective in [Zhang et al., 2022, Zhang et al., 2020]. The authors analyze the compressing sensing-based GF-NOMA via stochastic geometry in [Liu et al., 2021a]. A transmit power pool with the help of a deep reinforcement learning algorithm is created for UEs at certain distances sharing the same RB in [Fayaz et al., 2021]. In [Abbas et al., 2019] a novel framework is proposed to avoid collusion in GF-NOMA networks when two UEs choose the same pilot sequence. Index modulation integrated GF-NOMA scheme for uplink (UL) transmission is presented in [Doğan et al., 2019]. In [Celik, 2021], the author presents low com-

plexity multi-level and single GF-NOMA schemes and an UE clustering approach exploiting the channel gains of the UEs. RIS technology is used in [Chen et al., 2022] where authors propose a semi GF-NOMA scheme using deep reinforcement learning to control the transmit power and phase shifts. As pointed out by a recent survey on GF-NOMA [Shahab et al., 2020], RIS-aided GF-NOMA is a promising technology but has not been explored in-depth yet.

Chapter 3

A NEW RIS ARCHITECTURE WITH A SINGLE POWER AMPLIFIER: ENERGY EFFICIENCY AND ERROR PERFORMANCE ANALYSIS

In this chapter, we propose an amplifying RIS design that uses a single power amplifier. The proposed architecture includes two separated RISs and a power amplifier. The power amplifier receives the signal from a combiner circuit embedded in the first RIS, amplifies, and forwards it to the other one. The amplified signal is distributed among the reflecting elements of the second RIS and transmitted. Section 3.1 and Section 3.2 present the end-to-end system model of the proposed amplifying RIS design and the performance analysis of the system by investigating the BEP with a theoretical approach, respectively. In Section 3.3, the EE analysis is performed by considering the characteristics of the PAs. In Section 3.4, we exhibit our numerical results to evaluate the system performance.

3.1 System Model

In this section, we propose an amplifying RIS-assisted system model. In addition, a conventional passive RIS system model is given as the benchmark to the proposed scheme.

3.1.1 Amplifying RIS-assisted System

In this section, the considered single-input single-output (SISO) amplifying RIS-assisted system model is introduced. In this scenario, there are two passive RISs, denoted as RIS_1 and RIS_2, that are connected with a PA, and both have N number of reflecting elements while assuming there is no direct link between the Tx and

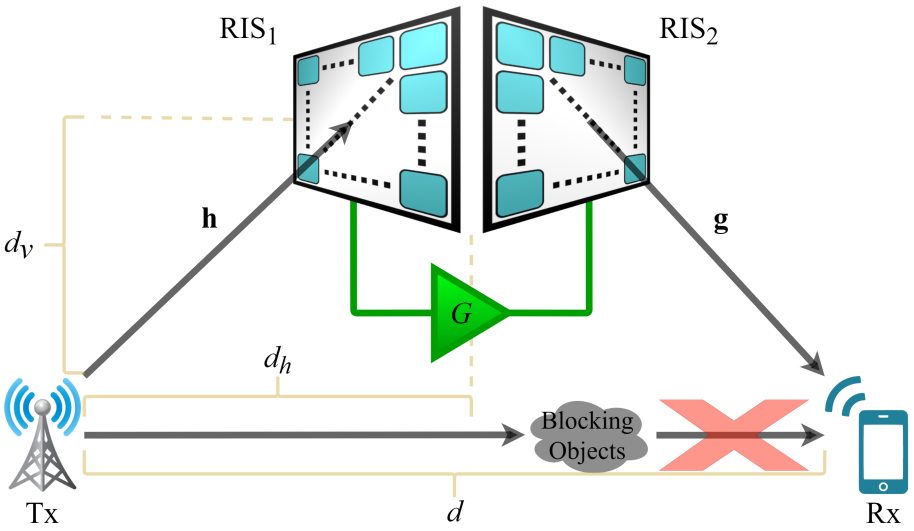

Figure 3.1: Generic system model for the considered amplifying RIS-assisted scheme.

Rx as shown in Fig. 3.1. The vertical and horizontal distances between the Tx and RISs, and the distance between the Tx and Rx are denoted as d_v, d_h and d, respectively. All of the reflecting elements of RIS_1 receive signals from the Tx and these signals are combined by RIS_1 to be directed to the PA as a single signal. Then, the signal is amplified by the PA by taking into account that there is also some additional noise to be amplified, which is due to all of the reflecting elements of RIS_1. Additionally, we consider the signal power at the output of the PA is limited. The system passes the resulting amplified signal through RIS_2, such that the reflecting elements of RIS_2 share and transmit the amplified signal. One should consider that there might be leakage from the signal transmitted by RIS_2 to the signal received by RIS_1. However, this issue can be resolved by properly positioning the RISs, since an RIS is an one-sided surface. In our design, RIS_1 and RIS_2 are placed back-to-back and separately as shown in Fig. 3.1, so that the signals directed by RIS_2 do not contaminate the signal captured by RIS_1.

In light of these, the received complex baseband signal can be expressed as

$$y = \sqrt{\frac{G}{N}} \left(\boldsymbol{\phi}^{\mathrm{T}} \mathbf{h} \sqrt{P_t} s + \sqrt{F} n_{\mathrm{tot}} \right) \boldsymbol{\theta}^{\mathrm{T}} \mathbf{g} + n_{\mathrm{rx}}, \tag{3.1}$$

where s, y, P_t, G, F, n_{tot}, and n_{rx}, correspond to the transmitted and received signals, transmit power at the Tx, the gain and noise figure of the PA, the total

amount of noise at the input of the PA, and the noise sample at the Rx, respectively. $\boldsymbol{\phi} \in \mathbb{C}^{N\times 1}$ and $\boldsymbol{\theta} \in \mathbb{C}^{N\times 1}$ are the reflecting element phase shift vectors of RIS_1 and RIS_2, respectively, where $\boldsymbol{\phi} = [\phi_1, \phi_2, \ldots, \phi_N]^{\text{T}}$, $\boldsymbol{\theta} = [\theta_1, \theta_2, \ldots, \theta_N]^{\text{T}}$, and ϕ_i and θ_i denote the phase shifts of the ith reflecting element of RIS_1 and RIS_2 for $i = 1, \ldots, N$, respectively. $\mathbf{h} \in \mathbb{C}^{N\times 1}$ is the channel between the Tx and RIS_1, where $\mathbf{h} = [h_1, h_2, \ldots, h_N]^{\text{T}}$, and h_i denotes the channel coefficient for Tx and ith reflecting element of RIS_1 for $i = 1, \ldots, N$. $\mathbf{g} \in \mathbb{C}^{N\times 1}$ is the channel between RIS_2 and the Rx, where $\mathbf{g} = [g_1, g_2, \ldots, g_N]^{\text{T}}$, and g_i represents the channel coefficient for ith reflecting element of RIS_2 and the Rx for $i = 1, \ldots, N$. Here, $\boldsymbol{\phi}^{\text{T}}\mathbf{h}\sqrt{P_t}s$ stands for the collected signal received by RIS_1. This signal is scaled by $\sqrt{G}$ with the help of the PA and divided by $\sqrt{N}$ due to the phase shift network of RIS_2 that is a kind of power-division circuit, so the total power is distributed among all of the reflecting elements of RIS_2. After that, the amplified and distributed signal is steered to the Rx with the help of RIS_2. A similar scenario is also valid for n_{tot}, so that it is multiplied with $\sqrt{F}$ and $\sqrt{G}$, then distributed among the reflecting elements of RIS_2. Here, the noise at RIS_2 is ignored, where the noise at RIS_1 is not because it is subject to amplification.

The channels exhibit either Rayleigh or Rician fading depending on the line-of-sight (LOS) probability, p_{LOS}, which is a function of the distance. The channel coefficients are modeled as

$$h_i = \sqrt{\frac{1}{\lambda^h}}\left(\sqrt{\frac{K_1}{K_1+1}}h_i^L + \sqrt{\frac{1}{K_1+1}}h_i^{NL}\right), \tag{3.2}$$

$$g_i = \sqrt{\frac{1}{\lambda^g}}\left(\sqrt{\frac{K_2}{K_2+1}}g_i^L + \sqrt{\frac{1}{K_2+1}}g_i^{NL}\right), \tag{3.3}$$

where K_1, K_2, λ^h, λ^g, h_i^L, g_i^L, h_i^{NL} and g_i^{NL} denote the Rician factors for Tx-RIS_1 and RIS_2-Rx links, the path loss, LOS and non-line-of-sight (NLOS) components for the channels $\mathbf{h}$ and $\mathbf{g}$, respectively, $h_i^{NL}, g_i^{NL} \sim \mathcal{CN}(0,1)$ for $i = 1, \ldots, N$, and $\mathcal{CN}(0,1)$ stands for the complex Normal distribution with zero mean and unit variance. If the channels do not include a LOS component, which mostly refers to Rayleigh fading,

we consider $K_1 = K_2 = 0$. Furthermore, the path loss components λ^h and λ^g depend on having NLOS or LOS links, and calculated as follows by considering the Indoor Hotspot (InH) environment in [3GP, 2019]:

$$\lambda_{\text{LOS}}[\text{dB}] = 32.4 + 17.3 \log_{10}(d_n) + 20 \log_{10}(f_c), \tag{3.4}$$

$$\lambda_{\text{NLOS}}[\text{dB}] = \max\left(\lambda_{\text{LOS}}, 32.4 + 31.9 \log_{10}(d_n) + 20 \log_{10}(f_c)\right), \tag{3.5}$$

where $d_n \in \{d_1, d_2\}$ depends on the channel, and $d_1 = \sqrt{d_v^2 + d_h^2}$, $d_2 = \sqrt{d_v^2 + (d - d_h)^2}$, and f_c are denoted as the distances between the Tx-RIS$_1$, RIS$_2$-Rx, and carrier frequency in GHz, respectively. The path loss components are the same for each h_i and g_i because the RIS is located in the far-field of the Tx and Rx. Furthermore, p_{LOS} for the InH environment is given as [3GP, 2019]

$$p_{\text{LOS}} = \begin{cases} 1, & d_n \leq 5, \\ e^{-\left(\frac{d_n - 5}{70.8}\right)}, & 5 < d_n \leq 49, \\ 0.54 e^{-\left(\frac{d_n - 49}{211.7}\right)}, & 49 < d_n. \end{cases} \tag{3.6}$$

To determine the SNR of the amplifying RIS-assisted sytem, (3.1) is expanded as

$$y = \sqrt{\frac{GP_t}{N}} \left(\boldsymbol{\phi}^{\text{T}} \mathbf{h}\right) \left(\boldsymbol{\theta}^{\text{T}} \mathbf{g}\right) s + \sqrt{\frac{GF}{N}} \left(\boldsymbol{\theta}^{\text{T}} \mathbf{g}\right) n_{\text{tot}} + n_{\text{rx}}. \tag{3.7}$$

From the received signal model given in (3.7), the SNR of the proposed system as follows:

$$\gamma_{\text{act}} = \frac{P_t \left| \sqrt{\frac{G}{N}} (\boldsymbol{\phi}^{\text{T}} \mathbf{h})(\boldsymbol{\theta}^{\text{T}} \mathbf{g}) \right|^2}{\left| \sqrt{\frac{GF}{N}} \boldsymbol{\theta}^{\text{T}} \mathbf{g} \right|^2 \sigma_{\text{tot}}^2 + \sigma_{\text{rx}}^2}, \tag{3.8}$$

where σ_{tot}^2 and σ_{rx}^2 are the noise powers at the input of the PA and Rx, respectively. γ_{act} is the instantaneous received SNR of the amplifying RIS-assisted system and the achievable rate of the system is expressed as $R_{\text{act}} = \log_2(1 + \gamma_{\text{act}})$.

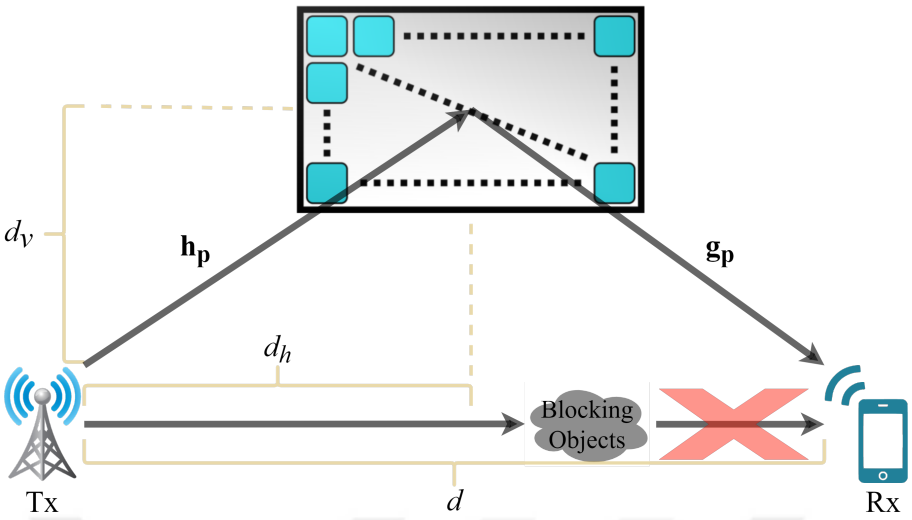

Figure 3.2: Generic system model for a passive RIS-assisted scheme.

3.1.2 Passive RIS-assisted System

This section is based on a passive RIS-assisted model shown in Fig. 3.2. In this scenario, only one RIS is used and it contains $2N$ reflecting elements such that it can be considered as a fair benchmark to the amplifying RIS-assisted model. The signal model of the passive system is specified as

$$y = \mathbf{g_p}^{\mathrm{T}} \mathbf{\Psi} \mathbf{h_p} \sqrt{P_t} s + n_{\mathrm{rx}}, \tag{3.9}$$

where $\mathbf{\Psi} \in \mathbb{C}^{2N \times 2N}$ is the reflecting element phase shift matrix of the RIS and $\mathbf{\Psi} = \mathrm{diag}\left(\left[\psi_1, \psi_2, \ldots, \psi_{2N}\right]\right)$ with ψ_i representing the phase shift for the ith element of the RIS for $i = 1, \ldots, 2N$. $\mathbf{h_p} \in \mathbb{C}^{2N \times 1}$ is the channel between the Tx and RIS, while $\mathbf{g_p} \in \mathbb{C}^{2N \times 1}$ stands for the channel between the RIS and Rx. They follow either Rician or Rayleigh fading depending on the distances to the Tx and Rx similar to the channels in the active model. Here, SNR of the passive model γ_{pas} is determined as

$$\gamma_{\mathrm{pas}} = \frac{P_t \left|\mathbf{g_p}^{\mathrm{T}} \mathbf{\Psi} \mathbf{h_p}\right|^2}{\sigma_{\mathrm{rx}}^2}, \tag{3.10}$$

where the achievable rate for the passive model is $R_{\mathrm{pas}} = \log_2\left(1 + \gamma_{\mathrm{pas}}\right)$.

3.2 Performance Analysis

In this section, we analyze the maximization of system capacity and the distribution of the received SNR for the amplifying RIS-assisted system, and present our theoretical BEP calculations accordingly. In order to maximize the system capacity, the received SNR for the amplifying RIS-assisted system should be maximized by finding optimum values of the phase shift vectors of RIS_1, RIS_2 and the gain of the amplifier G. The corresponding optimization problem is formulated as follows:

$$\begin{aligned}
\gamma_{\text{act}} = \max_{G,\boldsymbol{\phi},\boldsymbol{\theta}} \quad & \frac{P_t \left| \sqrt{\frac{G}{N}} (\boldsymbol{\phi}^{\mathrm{T}} \mathbf{h})(\boldsymbol{\theta}^{\mathrm{T}} \mathbf{g}) \right|^2}{\left| \sqrt{\frac{GF}{N}} \boldsymbol{\theta}^{\mathrm{T}} \mathbf{g} \right|^2 \sigma_{\text{tot}}^2 + \sigma_{\text{rx}}^2} \\
\text{s.t.} \quad & |\phi_i| = |\theta_i| = 1, \quad i \in \{1, 2, \ldots, N\}, \\
& G P_t \left| \boldsymbol{\phi}^{\mathrm{T}} \mathbf{h} \right|^2 \leq P_{\max}, \\
& G \leq G_{\max},
\end{aligned} \tag{3.11}$$

where $G_{\max}$ and $P_{\max}$ stand for the maximum gain of the amplifier and the maximum output power of the amplifier, respectively. Here, the optimal value of G depends on the phase shift matrix of RIS_1 as well. Therefore, the optimal solution to the phases of the reflecting elements should be determined first. The signals should be constructively combined at the PA and Rx to increase the received signal power. This can be done by eliminating the phases of the channels $\mathbf{h}$ and $\mathbf{g}$. The optimal solutions to reflecting element phases for RIS_1 and RIS_2 follow a constructive combining strategy [Wu and Zhang, 2019] by adjusting the phase shifts of the reflecting elements as:

$$\phi_i = e^{-j\angle h_i}, \tag{3.12}$$

$$\theta_i = e^{-j\angle g_i}, \tag{3.13}$$

where $\angle\cdot$ denotes the phase of a complex term. Next, we should specify the value for an optimal G by fixing the optimal value of $\boldsymbol{\phi}$ as in (3.12). It is mentioned earlier that there is a maximum power level for the amplified signal. Therefore, an

optimal gain value should be determined so that the power of the input signal to the amplifier, $P_{\text{in}} = P_t \left(\sum_{i=1}^{N} |h_i|\right)^2$, should not exceed the maximum output power when it is amplified. Thus, the equation below should be satisfied to obtain the optimal value of G;

$$\overline{G}_{\text{opt}} P_t \left(\sum_{i=1}^{N} |h_i|\right)^2 = P_{\max}, \tag{3.14}$$

where $\overline{G}_{\text{opt}}$ stands for the optimal gain value without the limitation of $G_{\max}$. Considering that $\overline{G}_{\text{opt}}$ can exceed $G_{\max}$, we define the optimal gain as:

$$G_{\text{opt}} = \min\left(\overline{G}_{\text{opt}}, G_{\max}\right). \tag{3.15}$$

By substituting G_{opt} in (3.15) to (3.8) for G and arranging the reflecting element phases of $\boldsymbol{\phi}$ and $\boldsymbol{\theta}$ as in (3.12) and (3.13), respectively, the maximized received SNR for the amplifying RIS-assisted system can be written as

$$\gamma_{\text{act}} = \frac{P_t \frac{P_{\max}}{N} A^2 B^2}{\frac{P_{\max} F}{N} B^2 \sigma_{\text{tot}}^2 + P_t A^2 \sigma_{\text{rx}}^2}, \tag{3.16}$$

where $A = \sum_{i=1}^{N} |h_i|$ and $B = \sum_{i=1}^{N} |g_i|$. Here, one can easily observe that the maximized received SNR increases proportional to N, P_t, and $P_{\max}$. However, there are also other constraints that can limit the effect of the RIS size and the Tx power, such as $P_{\max}$ and $G_{\max}$. The effects of these constraints are further investigated in Section V. Moreover, the amplifying RIS model experiences multiplicative path loss just like the passive RIS since (3.16) includes the multiplication of A and B. Nevertheless, the gain factor significantly compensates this double path loss effect.

Probability analysis of the maximized SNR in (3.16) gives us useful insights. The terms A and B converge to Gaussian distributed random variables due to the Central Limit Theorem (CLT) for sufficiently large N, where $|h_i|$ and $|g_i|$ are Rayleigh or Rician distributed random variables. Thus, A^2 and B^2 follow non-central chi-square distribution with one degree of freedom. The denominator and numerator of the SNR term in (3.16) are correlated and follow Gamma distribution due to the combination of weighted non-central chi-square random variables. The received SNR

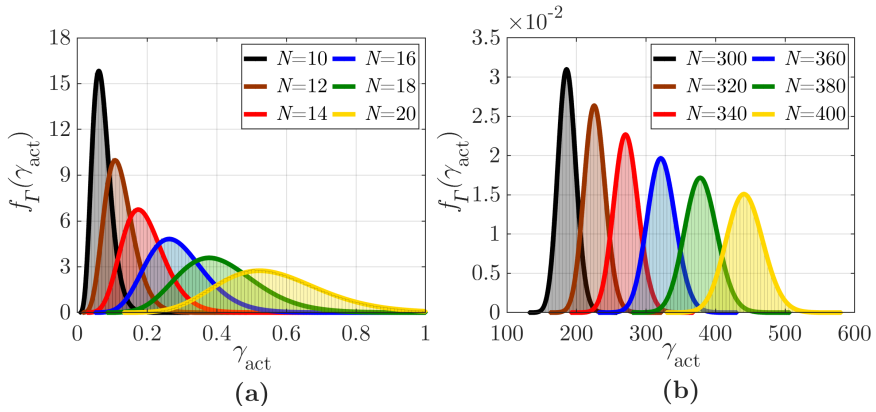

Figure 3.3: The PDF of γ_{act} and Gamma distribution fits for (a) $N = 10, \ldots, 20$ and (b) $N = 300, \ldots, 400$.

term in (3.16) becomes the ratio of two correlated Gamma random variables and therefore, subject to the Gamma distribution [Flueck and Holland, 1973]. To the best of the authors' knowledge, although there are a number of articles in the literature examining the ratio of two Gamma random variables and ratio of correlated chi-square random variables, no studies pointing to this kind of distribution has been found[Joarder, 2009, Lee et al., 1979, Provost and Rudiuk, 1994]. Therefore, using Open Distribution Fitter app (dfittool), we can find the Gamma parameters of the received SNR distribution on MATLAB and prove that it follows the Gamma distribution.

The distribution of γ_{act} is investigated for different N values as seen in Fig. 3.3. Histograms represent the distributions of γ_{act} and are obtained by performing Monte Carlo simulations. The overlapping lines stand for the fitted Gamma distributions. The Gamma distribution fits exactly to the probability density function (PDF) of γ_{act}. Thus, the PDF of γ_{act} can be written as[Lee et al., 1979]

$$f_\Gamma(\gamma_{\text{act}}) = \frac{\gamma_{\text{act}}^{k-1} e^{-\gamma_{\text{act}}/\nu}}{\nu^k \Gamma(k)}, \tag{3.17}$$

where $\Gamma(\cdot)$, k, and ν represent the Gamma function, shape, and scale parameters, respectively. The shape and scale parameters for the fitted Gamma distribution are provided in Table A.1 for various system specifications[1]. The parameters of the

[1]Interested readers can produce arbitrary results as well by using the source code provided:

Gamma distribution vary for different specifications such as N, $P_{\max}$ and P_t. For instance, the standard deviation of the distribution increases with N as shown in Fig. 3.3.

Theoretical symbol error probability (SEP) is calculated by using the moment generation function of the Gamma distribution as follows [Arslan et al., 2022]:

$$M_{\gamma_{\text{act}}}(s) = (1 - \nu s)^{-k}, \text{ for } s < \frac{1}{\nu}. \tag{3.18}$$

The average SEP for M-ary phase-shift keying (M-PSK) signaling by using the moment generation function in (3.17) is given as follows:

$$P_s = \frac{1}{\pi} \int_0^{(M-1)\pi/M} M_{\gamma_{\text{act}}} \left(\frac{-\sin^2(\pi/M)}{\sin^2 x} \right) dx. \tag{3.19}$$

We can numerically calculate the SEP in (3.19) by using the Gamma distribution parameters and obtain BEP as $P_e \approx P_s/\log_2 M$. Accordingly, the BEP for binary phase-shift keying (BPSK) simplifies to

$$P_e = \frac{1}{\pi} \int_0^{\pi/2} \left(1 + \frac{\nu}{\sin^2 x} \right)^{-k} dx. \tag{3.20}$$

3.3 Total Power Consumption Model and Energy Efficiency Analysis

In this section, we present power consumption models for the proposed amplifying and passive RIS designs, and we analyze and compare the EE for both systems. The main power consuming elements can be listed as transmitter, receiver, amplifiers and RIS elements. There are two PAs in the system, one at the Tx and one between the RISs. We assume ideal PAs whose power efficiency is given as [Makki et al., 2015a]

$$\frac{P_{\text{out}}}{P_{\text{amp}}} = \eta_{\max} \left(\frac{P_{\text{out}}}{P_{\max}} \right)^{\varepsilon}, \tag{3.21}$$

where P_{amp} and P_{out} correspond to power consumed by the amplifier and the output power of the amplifier, respectively. The maximum output power of the amplifier

https://github.com/recepakiftasci/Amplifying-RIS

is set to $P_{\max}$ to ensure that it operates in the linear region. Here, $\eta_{\max} \in (0, 1]$ is the maximum efficiency of the amplifier and ε is a parameter that depends on the amplifier class. We assume $\varepsilon = 0.5$ for more accurate modeling as in [Persson et al., 2013]. The power consumed by the PA can be obtained by reorganizing (3.21) as

$$P_{\text{amp}} = \frac{1}{\eta_{\max}} \sqrt{P_{\text{out}} P_{\max}}. \tag{3.22}$$

The phase shift of each RIS element is arranged by programmable electronic circuits that consume power as well. The power consumption of the RIS depends on the phase resolution of RIS elements [Jia et al., 2021] and modeled as

$$P_{\text{RIS}} = N P_n(b), \tag{3.23}$$

where $P_n(b)$ is the power consumption of each RIS element which is a function of bit-resolution. We consider 6-bit phase resolution for each RIS element, which consumes 7.8 mW power according to [Huang et al., 2019]. The total power consumption of the amplifying RIS-assisted system is expressed as follows:

$$P_{\text{tot}}^{\text{act}} = \alpha P_t + P_{\text{Tx}} + P_{\text{Rx}} + N P_n(b) + \beta \sqrt{P_{\text{out}} P_{\max}}, \tag{3.24}$$

where $\alpha = \omega_{\max}^{-1}$ and $\beta = \eta_{\max}^{-1}$ with $\omega_{\max}$ and $\eta_{\max}$ represent the maximum efficiency of the transmit PA and the PA between the RISs, respectively. We assume that $P_t = P_{\max}$ for the transmit PA. Here, P_{Tx} and P_{Rx} are the hardware dissipated static powers at Tx and Rx, respectively and therefore they are constant and do not depend on the system parameters. The values for the power consumption model parameters are given in Table 3.1 as stated in [Huang et al., 2019]. Likewise, the power consumption of the passive RIS-assisted system can be written as follows only by omitting the power consumed by the PA between the RISs:

$$P_{\text{tot}}^{\text{pas}} = \alpha P_t + P_{\text{Tx}} + P_{\text{Rx}} + N P_n(b), \tag{3.25}$$

The bit-per-joule energy efficiency (η_{EE}) of a system can be expressed as

$$\eta_{\text{EE}} = \frac{R_i BW}{P_{\text{tot}}^{i}}, \tag{3.26}$$

Table 3.1: Power consumption model parameters

Parameter	**Value**
α	1.2
β	1.2
$P_n(b)$	7.8 mW
P_{Tx}	9 dBW
P_{Rx}	10 dBm

where BW is the communication bandwidth, R_i is the achievable rate, and P^i_{tot} is the total consumed power by the system where $i \in \{\text{act}, \text{pas}\}$. The amplifying RIS-assisted system consumes more power but provides higher capacity in return. On the other hand, passive RIS-assisted system is less power consuming and provides less capacity due to its fully passive nature. The EE analysis is an important criterion determining which system performs better in terms of energy consumption. We compute EE for different systems through computer simulations without particularly focusing on the optimization of the EE.

3.4 Numerical Results

In this section, we provide numerical results for both the amplifying and passive RIS models to evaluate and compare the performances of them under several configurations. Achievable rate, bit error rate (BER), power consumption, and EE have been presented by computer simulations and discussed in detail. We consider the systems as shown in Figs. 3.1 and 3.2 with parameters d_v = 5 m, d_h = 5 m, d = 50 m, P_t = 30 dBm, $P_{\max}$ = 30 dBm, f_c = 28 GHz, BW = 180 kHz, F = 5 dB, $K_1 = K_2 = 5$, N = 128, $n_{\text{rx}} = n_{\text{tot}} = -100$ dBm, and $G_{\max}$ = 30 dB, unless specified otherwise[Analog Devices, a, Sarkar et al., 2017, Analog Devices, b]. Achievable rate and EE simulations are performed with 10^6 iterations.

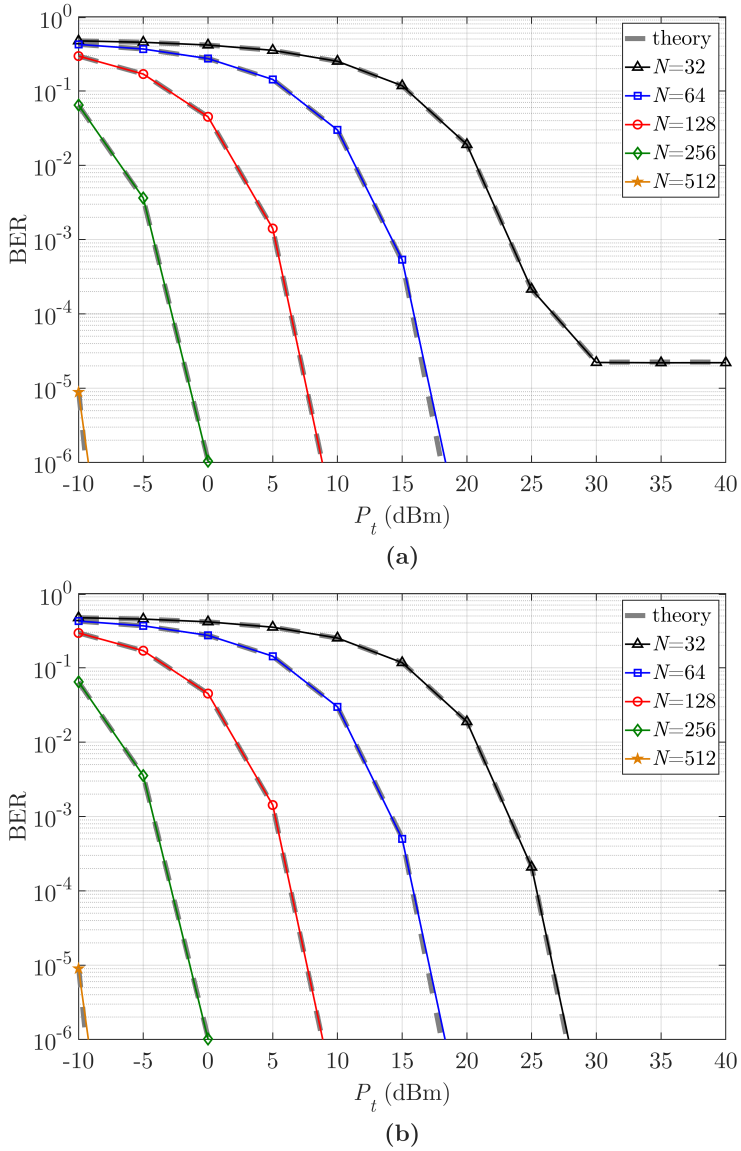

Figure 3.4: BER results for (a) $P_{\max}$ = 10 dBm and (b) $P_{\max}$ = 20 dBm.

3.4.1 Performance Evaluation

In this subsection, numerical results for BER and achievable rate are presented. For the BER analysis, two different setups with $P_{\max}$ = 10 dBm and $P_{\max}$ = 20 dBm are considered. Fig. 3.4(a) shows the BER performance when $P_{\max}$ = 10 dBm, while Fig. 3.4(b) exhibits the results for $P_{\max}$ = 20 dBm. Here, the corresponding theoretical values are given, as well. From Fig. 3.4(a), one can easily observe that an error floor occurs after P_t = 25 dBm for N = 32 case. On the other hand, an error floor is not observed in Fig. 3.4(b). This is because of the limitation of P_{out}

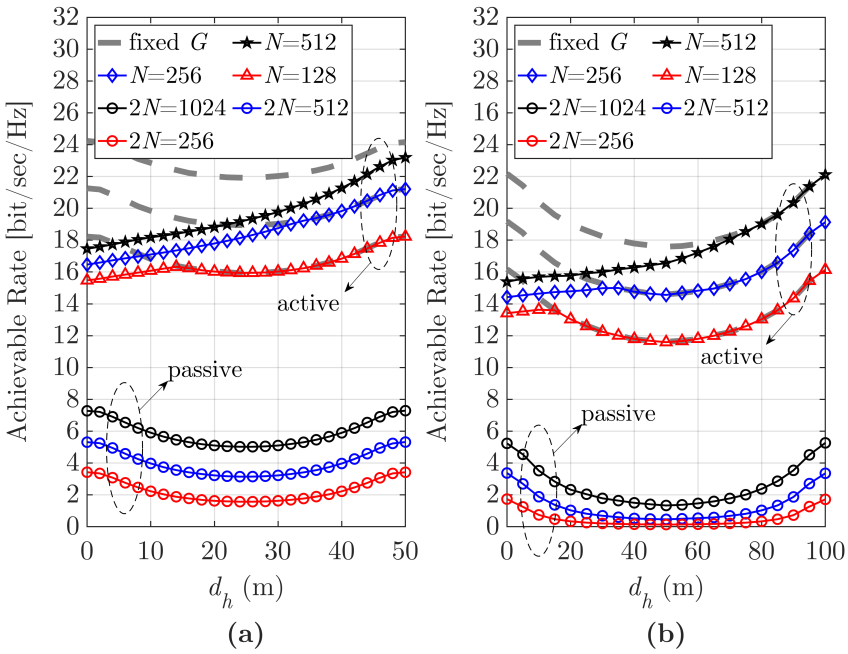

Figure 3.5: Achievable rates of the system for (a) $d_h = 50$ m and (b) $d_h = 100$ m.

when the input signal becomes too strong such that the amplifier cannot stay in the linear region if it continues to enhance the signal with the current gain. In this case, when P_{out} is fixed to $P_{\max}$, further increment in P_t does not lead a better error performance after a certain point, and thus we observe an error floor. On the other hand, in Figs. 3.4(a) and (b) we do not observe any error floor when P_{out} is smaller than $P_{\max}$. Furthermore, the better BER performance is achieved with larger N and higher P_t in both cases as long as P_{out} does not reach $P_{\max}$. Based on these investigations, we can conclude that it may be beneficial to keep $P_{\max}$ high enough to prevent any error floor. In addition, it should be emphasized that using a larger RIS can further strengthen the received signal and an error floor appears for lower P_t values due to the limitation of P_{out}.

Achievable rates of both designs for varying d_h with several N values are presented in Fig. 3.5. For this figure, the lines labeled as $N = 128$, 256, and 512 represent the achievable rates for the active model, where those labeled with $2N = 256$, 512, and 1024 stand for the passive model. The dashed lines show the performance behaviours when there is not any output power limitation for the amplifier (i.e., results with a fixed G value of 30 dB). In Fig. 3.5(a), the achievable rates for

the active model overlap with the corresponding dashed lines when $P_{\text{out}} \leq P_{\max}$ and $G_{\text{opt}} = G_{\max}$. We observe that the intersection points with the dashed lines occur at smaller values of d_h as N decreases. The reason behind is that G_{opt} begins to decrease after the intersection points as the amplifying RIS gets closer to the Tx to keep $P_{\text{out}} = P_{\max}$. Moreover, it is a well known fact that placing an RIS close to the Tx or Rx results in a better system performance. This can be seen in both the Figs. 3.5(a) and (b), however, that is not the case with the amplifying RIS design. Placing the amplifying RIS close to the Tx provides lower achievable rates. We mentioned earlier that the reason behind this is the limitation of P_{out} and having a greater $P_{\max}$ would be a solution to this problem. Based on these examinations, one can conclude that the amplifying RIS can overcome the common problem that generally affects system performance unpleasingly in passive RIS designs, which is the necessity of placing the RIS close to the Tx or Rx. As seen in Fig. 3.5(a), the worst achievable rate is obtained when the RIS is placed in the middle of the Rx and Tx for the passive RIS. This gets even worse in Fig. 3.5(b) when the Tx and Rx are further apart. The amplifying RIS design significantly reduces the multiplicative path loss effect by amplifying the combined signal by RIS_1 as it uses a PA between the two RISs. Using the amplifying RIS instead of the passive one can compensate this performance drop, even enhance the performance further.

Similar to passive RIS scenarios, the RIS size has a considerable impact on achievable rate also for the active RISs. Fig. 3.6 illustrates the achievable rates of the amplifying RIS design where Figs. 3.6(a) and (b) stand for $P_t = 20$ dBm and $P_t = 10$ dBm, respectively. Here, the numbers for each marker signify G_{opt} for corresponding N. Here, G_{opt} begins to decrease after a point for all of the cases except for $P_{\max} = 20$ dBm in Fig. 3.6(b). Different from the previous case, the reason behind the occurrence of the break points is the bigger N values, such that P_{in} increases if more reflecting elements are used and again limits G_{opt}. In Fig. 3.6(a), P_{out} reaches $P_{\max}$ for large N and amplifier cannot operate with $G_{\max}$ even if $P_{\max} = 20$ dBm. However, when P_t is reduced to 10 dBm as in Fig. 3.6(b), we see that P_{out} cannot reach $P_{\max} = 20$ dBm even for large N and the amplifier can boost the signal with $G_{\max}$.

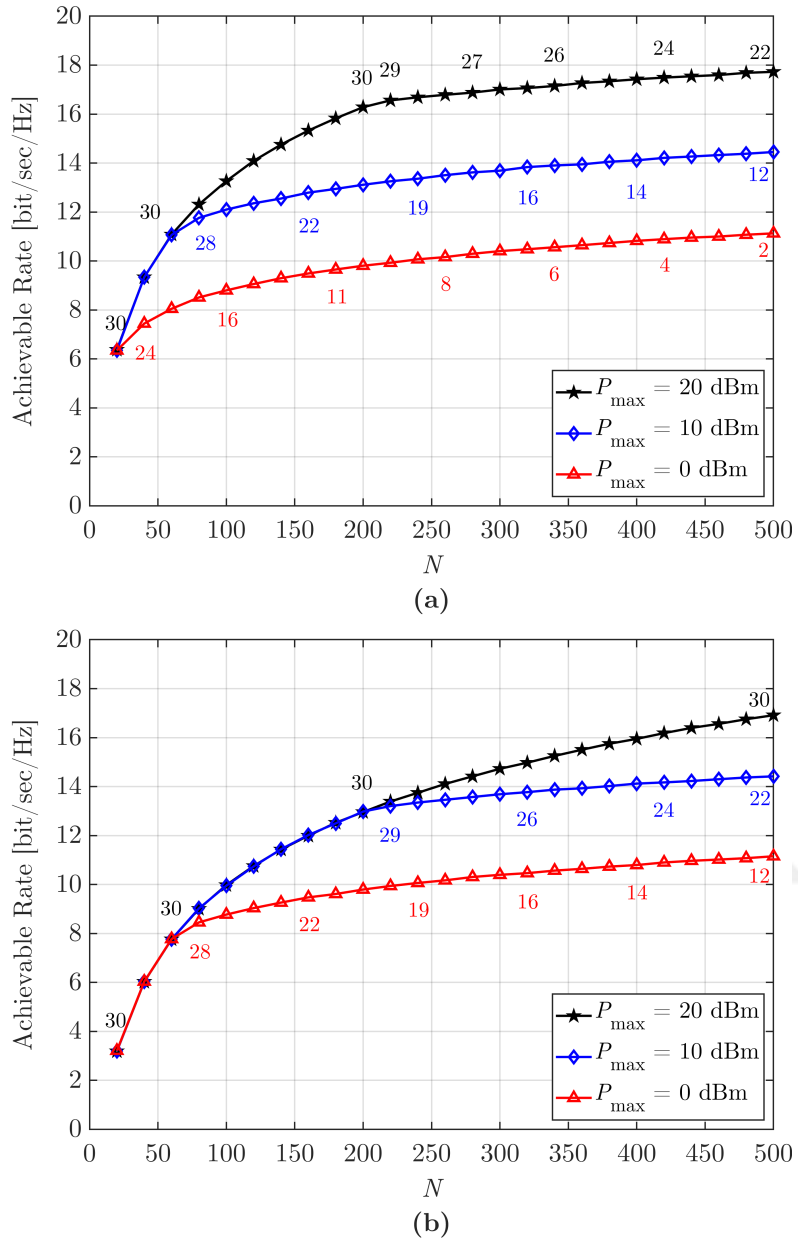

Figure 3.6: Achievable rates of the amplifying RIS-assisted system for (a) P_t = 20 dBm and (b) P_t = 10 dBm. The numbers on the markers indicate G_{opt} values.

Tx power and RIS size cause similar effects on the system performance because both of them enhance P_{in}. As seen from Figs. 3.6(a) and (b), increasing P_t does not always have an extra constructive effect on the system capacity because the achievable rates become identical for the same $P_{\max}$ after a certain point as clearly demonstrated in Fig. 3.7 as well. In Fig. 3.7, the achievable rates are the same after $N = 200$ and $N = 60$ when $P_{\max} = 20$ dBm and $P_{\max} = 10$ dBm, respectively, because

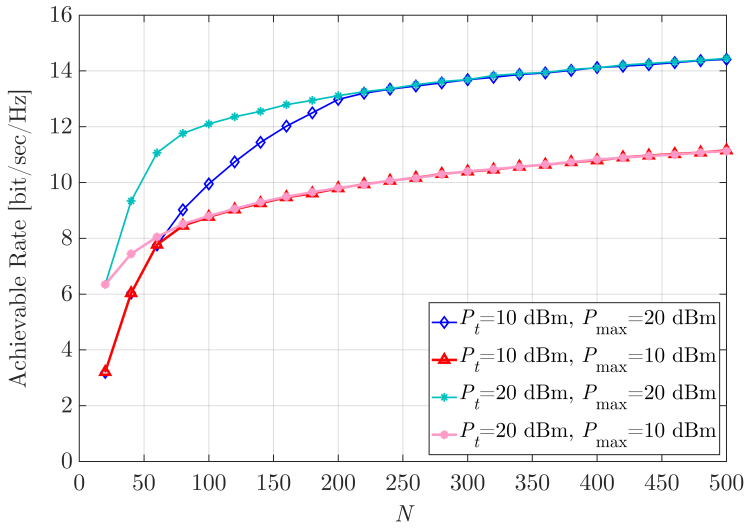

Figure 3.7: Achievable rates of the amplifying RIS-assisted system for different P_t and $P_{\max}$.

$P_{\text{out}} = P_{\max}$ at these N values. Since $P_{\max} = 10$ dBm can be reached by lower P_{in} values, the intersection point occurs at lower N compared to the case $P_{\max} = 20$ dBm. On the other hand, a considerable performance difference is examined where N is smaller than 100 and 50 for $P_{\max} = 20$ dBm and $P_{\max} = 10$ dBm, respectively. These observations indicate that the system performance is not enhanced with P_t after the break points, nevertheless, it can be boosted slightly by using larger N. This can be explained by the fact that there are two RISs at both sides of the amplifier. Increasing N for RIS_1 can enhance P_{in} just as P_t, however, P_{out} will be the same if it is already at $P_{\max}$, so this increment in N for RIS_1 does not affect the achievable rate. Despite this, if more reflecting elements are used for RIS_2, slightly higher achievable rates are achieved although the total power is the same such that it is distributed among those reflecting elements. The reason of this advance is the beamforming gain which increases with N.

Considering the results presented in this subsection, the main performance limiting factors are the PA parameters, which are $P_{\max}$ and $G_{\max}$. Therefore, N and P_t has a considerable effect on the performance depending on the PA parameters.

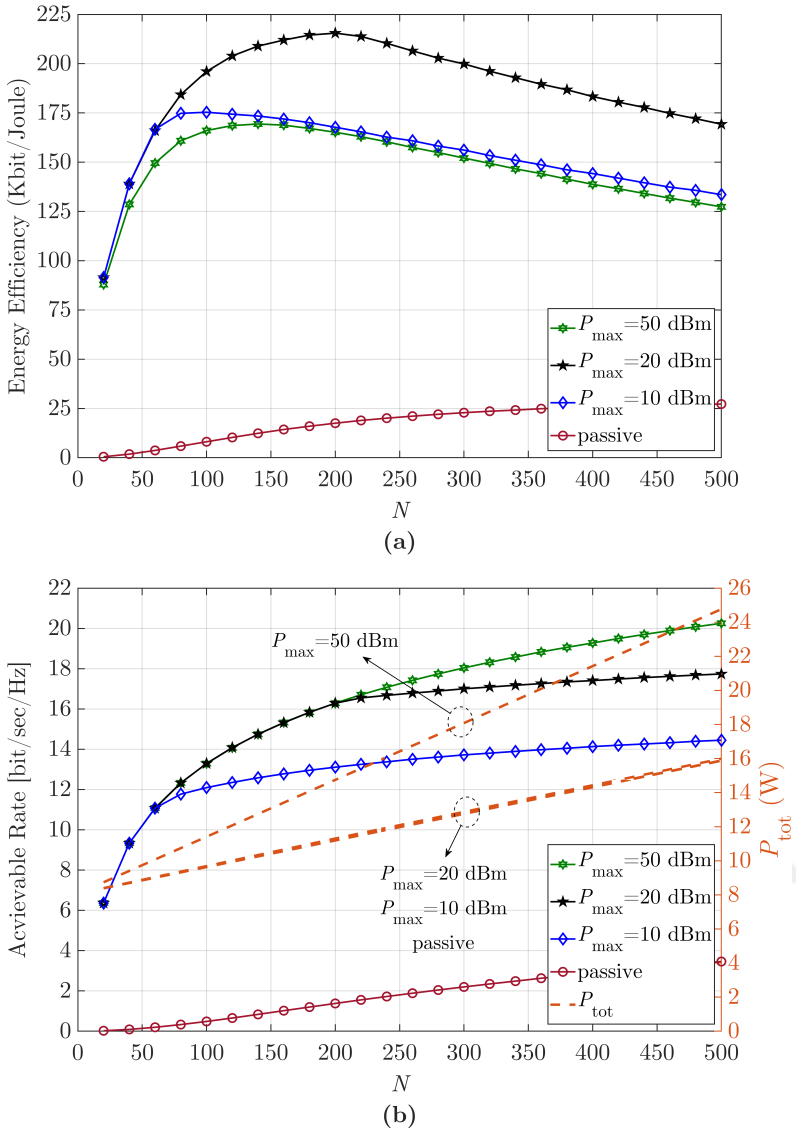

Figure 3.8: (a) Energy efficiencies of the amplifying RIS-assisted system for varying N and (b) corresponding achievable rates and P_{tot} values

3.4.2 Energy Efficiency Evaluation

In this subsection, numerical results for EE and power consumption are presented. Fig. 3.8(a) shows the EE values for varying N and different $P_{\max}$ values where Fig. 3.8(b) stands for the corresponding achievable rates and P_{tot}. In Fig. 3.8(a), the EE values start to decline after some points because the achievable rates are almost at a constant level for $P_{\max}$ = 20 dBm and $P_{\max}$ = 10 dBm while P_{tot} is still increasing as seen in the Fig. 3.8(b). When $P_{\max}$ = 50 dBm, a worse EE performance is

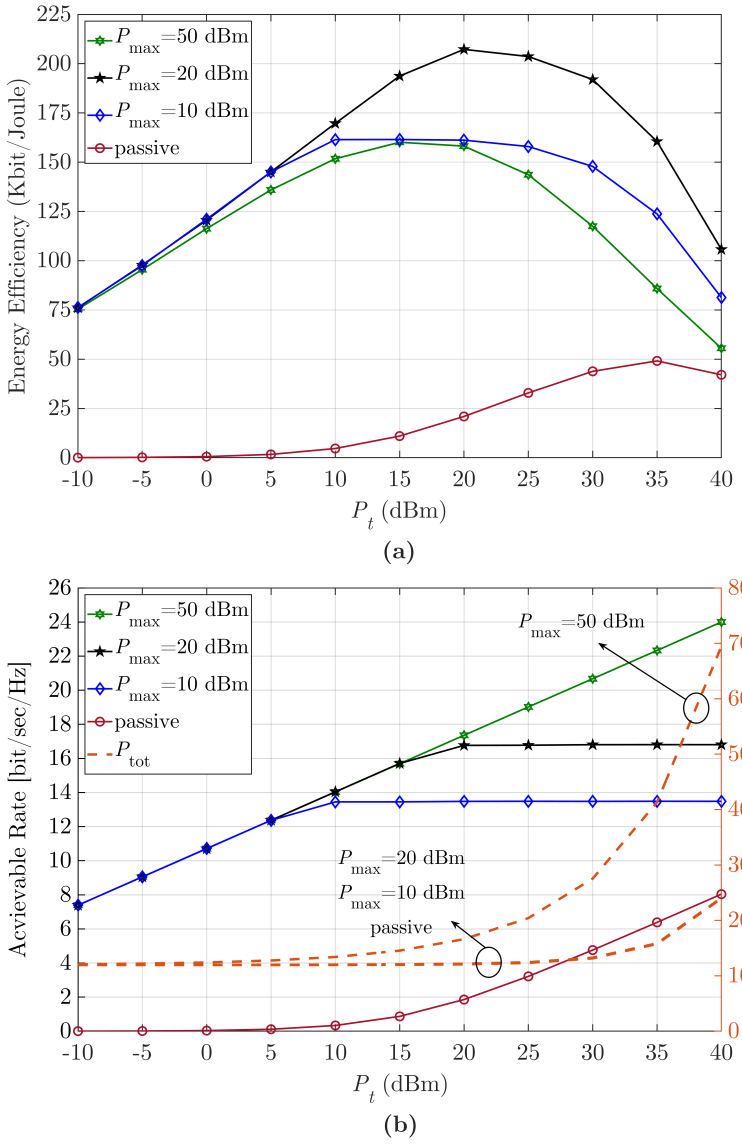

Figure 3.9: (a) Energy efficiencies for different $P_{\max}$ values varying with P_t and (b) corresponding achievable rates and P_{tot} values

obtained as the increase in power consumption has a greater effect than the increase in the achievable rate. Unless $P_{\max}$ is too high, the total power consumption of the active design is nearly the same as the passive RIS. Consequently, the active design performs better in terms of EE.

EE is investigated for varying P_t and different $P_{\max}$ values in Fig. 3.9(a). Achievable rates and P_{tot} values are also given in Fig. 3.9(b) for the same scenario. For $P_{\max}$ = 20 dBm and $P_{\max}$ = 10 dBm, although the amplifying RIS does not consume high amount of power, the EE begins to decrease after some points. The reason is

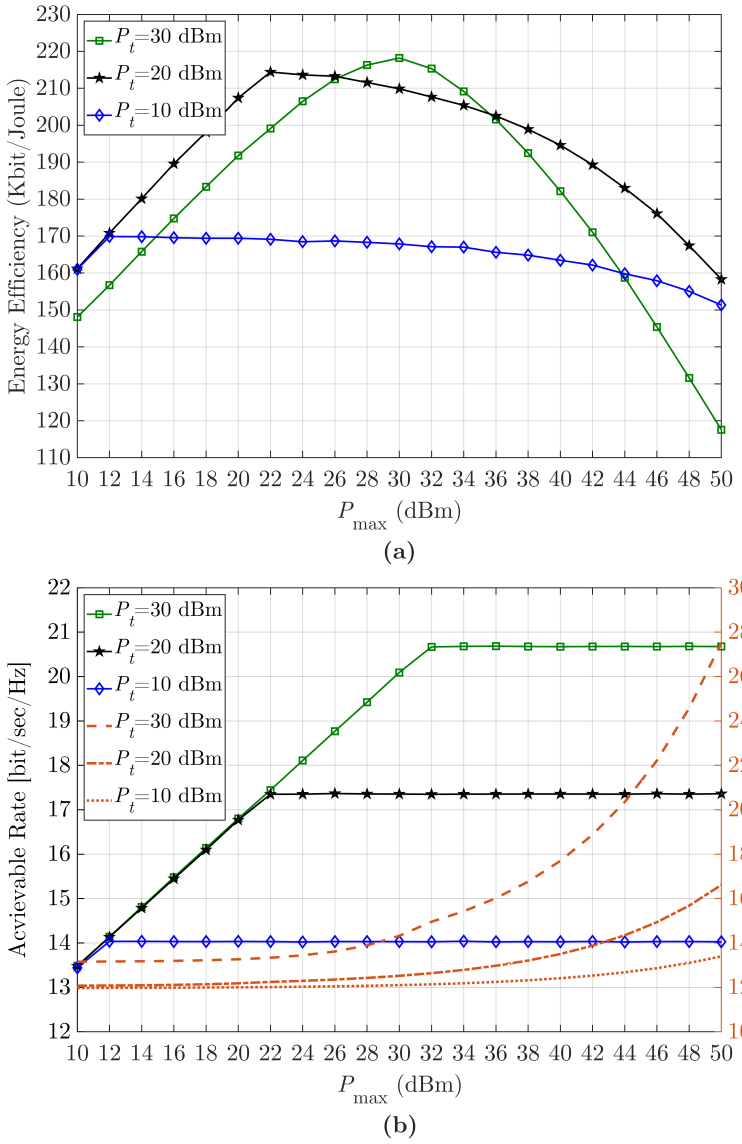

Figure 3.10: (a) Energy efficiencies for different P_t values varying with $P_{\max}$ and (b) corresponding achievable rates and P_{tot} values

that increasing P_t after these points does not affect the achievable rate, but increases P_{tot}. For the case of $P_{\max} = 50$ dBm, as we do not reach $P_{\max}$, both the power consumption of the PA at the base station and the PA between the RISs increases. Accordingly, we observe that the EE starts to decrease after a certain point even if the achievable rate keeps increasing.

Finally, Figs. 3.10(a) and (b) represent the EE, achievable rate, and P_{tot} for varying P_t and different $P_{\max}$ values. Unlike Figs. 3.8 and 3.9, the break points occur when the amplifier cannot amplify the signal more than $G_{\max} = 30$ dB. Thus,

increasing the $P_{\max}$ only leads to higher power consumption as explained in (3.22) while it does not have a positive effect on the achievable rate. This causes the EE to show an interesting downward trend.

In the view of these observations, one can conclude that the EE is affected by many parameters such as P_t, $P_{\max}$, N, and $G_{\max}$. As shown in (3.22), $P_{\max}$ and P_t have a more clear effect on the EE compared to the other parameters. Increasing these parameters to have a higher achievable rate does not always lead to a more energy efficient system. To reach a system with a maximum EE, all of these parameters should be jointly optimized, which requires advanced optimization techniques and might be a topic for the future works.

Chapter 4

RIS-ASSISTED GRANT-FREE NOMA: USER PAIRING, RIS ASSIGNMENT, AND PHASE SHIFT ALIGNMENT

In this chapter, a RIS-assisted GF-NOMA scheme is proposed. We realize that using active RISs to assist NOMA systems can be a very promising approach to boost the system performance. For that reason, we assist a GF-NOMA network with fully-connected active RISs. Section 4.1 presents the considered network and channel model, the proposed signal model and the RIS phase alignment process. Section 4.2 provides the problem formulation and briefly explains the proposed solution methodologies. Section 4.3 introduces proposed UE clustering, RIS assignment, and phase shift alignment approaches. At the end of this chapter, Section 4.4 presents the benchmark schemes and numerical results.

4.1 System Model

In this section, we introduce the considered system model in four subsections. In Section 4.1.1, the architecture of the network is demonstrated by addressing the UE distribution as well as RIS deployment and partitioning. In Section 4.1.2, the channel model is exhibited in detail. The signal models and SINRs of the passive and active RIS-assisted schemes are given in Section 4.1.3 and 4.1.4, respectively.

4.1.1 Network Model

We consider UL operation of a network consisting of a single BS serving U UEs over R RBs with W [Hz] bandwidth, whose sets are denoted by $\mathcal{U}$ and $\mathcal{R}$, respectively. All UEs operate at an identical power, p_{id}, which is broadcast by the BS over a control channel. Without loss of generality, UEs are assumed to be uniformly distributed over a cell area of radius D. To show the proposed GF-NOMA schemes' suitability

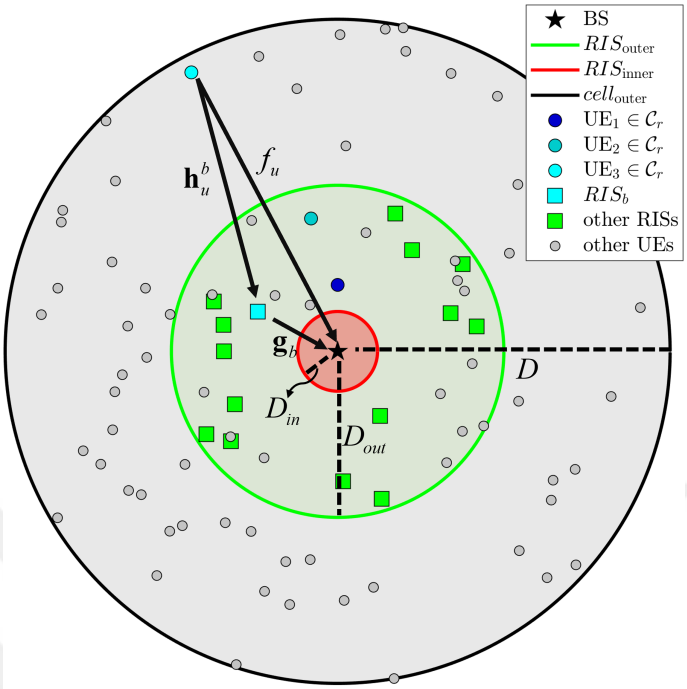

Figure 4.1: Outer and inner cells of the network

for massive connectivity, we consider a dense network scenario (i.e., $U \gg R$) and group/cluster multiple UEs to utilize a single RB. That is, the number of clusters C is the same with R, and RB/cluster terms are used interchangeably throughout the thesis. Even though R and C are fixed, U can dynamically change according to spatio-temporal characteristics of the network traffic. Hence, the UE density dependent maximum cluster size is set as $K = \lceil \frac{U}{R} \rceil$. Accordingly, the cluster set utilizing RB_r is defined by $\mathcal{C}_r = \{\text{UE}_u \mid \chi_r^u = 1, \forall u \in \mathcal{U}, \sum_{u \in \mathcal{U}} \chi_r^u \leq K\}$, where χ_r^u is the binary UE clustering indicator, i.e., $\chi_r^u = 1$ if UE_u belongs to rth cluster, otherwise $\chi_r^u = 0$.

In order to improve network performance and facilitate the GF-NOMA, M RISs are uniformly deployed in a disk having inner and outer radius of D_{in} and D_{out}, $D_{\text{in}} \leq D_{\text{out}} \leq D$, where D_{in} ensures that RISs are placed at the far-field of the BS as shown in Fig. 4.1. Each physical RIS is partitioned into G logical sub-blocks, each with N elements, resulting in an overall $B = MG$ RIS blocks. Each block can

be exploited by a member of a cluster, and a cluster cannot be assigned to more than one block. Accordingly, the set of RIS blocks is denoted by $\mathcal{B}$, and the bth RIS block is denoted by RIS_b. The binary RIS assignment matrix is denoted by $\mathbf{\Delta} \in \{0,1\}^{B\times U\times R}$ with entries $\delta^u_{r,b}$ such that $\delta^u_{r,b} = 1$ if RIS_b is assigned to the rth cluster and configured based on the channels of $\text{UE}_u \in \mathcal{C}_r$, $\delta^u_{r,b} = 0$ otherwise. Fig. 1.2 demonstrates the RIS assignment and phase shift alignment for two different type of UEs. Even though $\text{UE}_u \in \mathcal{C}_r$ has a LoS link to the BS, RIS_b is aligned to its channel to further improve the sum rate of $\mathcal{C}_r$. On the other hand, $\text{RIS}_{b'}$ is aligned to provide coverage to $\text{UE}_{u'} \in \mathcal{C}_{r'}$, whose LoS link to the BS is blocked by a building.

4.1.2 Channel Model

The channels are modeled according to the Urban Macro (UMa) scenario of the 3GPP standard specified for 0.5-100 GHz bands [3GP, 2019]. The channel between UE_u and RIS_b is denoted by $\mathbf{h}^b_u = \left[h^1_{u,b}, \ldots, h^n_{u,b}, \ldots, h^N_{u,b}\right] \in \mathbb{C}^{N\times 1}$, where $h^n_{u,b}$ is the channel coefficient from UE_u to nth reflecting element of the RIS_b, $n \in [1, N]$. Similarly, the channel vector between the BS and RIS_b is denoted by $\mathbf{g}_b = \left[g^1_b, \ldots, g^n_b, \ldots, g^N_b\right] \in \mathbb{C}^{N\times 1}$, where g^n_b is the channel coefficient between the BS and nth reflecting element of the RIS_b, $n \in [1, N]$. Moreover, the direct channel from UE_u to the BS is denoted by $f_u \in \mathbb{C}$. All these channels are assumed to experience Rayleigh and Rician fading under line-of-sight (LoS) and non-line-of-sight (NLoS) conditions, respectively. The channel coefficients are modeled as

$$h^n_{u,b} = \sqrt{\frac{1}{\lambda_h}}\left(\sqrt{\frac{K_h}{K_h+1}}h^{n,\text{LoS}}_{u,b} + \sqrt{\frac{1}{K_h+1}}h^{n,\text{NLoS}}_{u,b}\right), \tag{4.1}$$

$$g^n_b = \sqrt{\frac{1}{\lambda_g}}\left(\sqrt{\frac{K_g}{K_g+1}}g^{n,\text{LoS}}_{b} + \sqrt{\frac{1}{K_g+1}}g^{n,\text{NLoS}}_{b}\right), \tag{4.2}$$

$$f_u = \sqrt{\frac{1}{\lambda_f}}\left(\sqrt{\frac{K_f}{K_f+1}}f^{\text{LoS}}_{u} + \sqrt{\frac{1}{K_f+1}}f^{\text{NLoS}}_{u}\right), \tag{4.3}$$

where $K_h/K_g/K_f$ is the Rician factor for $\mathbf{h}^b_u/\mathbf{g}_b/f_u$; $\lambda_h/\lambda_g/\lambda_f$ is the path loss over $\mathbf{h}^b_u/\mathbf{g}_b/f_u$; $h^{n,\text{LoS}}_{u,b}/g^{n,\text{LoS}}_b/f^{\text{LoS}}_u$ is the LoS component; and $h^{n,\text{NLoS}}_{u,b}/g^{n,\text{NLoS}}_b/\ f^{\text{NLoS}}_u \sim$

$\mathcal{CN}(0,1)$ is the NLoS component of $\mathbf{h}_u^b/\mathbf{g}_b/f_u$. If a channel does not include a LoS component, which mostly refers to Rayleigh fading, we consider the corresponding Rician factor as 0. λ_h, λ_g, and λ_f can be calculated as per LoS or NLoS links depending on the LoS probability given in [3GP, 2019, Table 7.2-2]. Additionally, the path loss models and the Rician factors are calculated and obtained according to the UMa scenario of the 3GPP standard [3GP, 2019, Table 7.2-1].

4.1.3 Passive RIS-Assisted NOMA System

Based on UE-RIS-BS cascaded channels and UE-BS channels defined in the previous subsection, the received complex baseband signal of the proposed system at the BS over RB_r when passive RISs are used can be expressed as

$$y_{r_{\mathrm{pas}}}(\boldsymbol{\Delta}) = \sqrt{p_{\mathrm{id}}}\left(\sum_{\forall u \in \mathcal{C}_r}\sum_{\forall k,l,m} \underbrace{\mathbf{g}_l^{\mathrm{T}}\left(\boldsymbol{\Phi}_{k,l}^m \delta_{k,l}^m\right)\mathbf{h}_u^l s_u}_{\text{UEs-RIS-BS}} + \underbrace{f_u s_u}_{\text{UEs-BS}}\right) + n, \tag{4.4}$$

where $k \in \mathcal{R}$; $l \in \mathcal{B}$; $m \in \mathcal{U}$; $y_{r_{\mathrm{pas}}}(\boldsymbol{\Delta})$ is the received signal from members of $\mathcal{C}_r$ at RB_r; s_u is the symbol transmitted by $\mathrm{UE}_u \in \mathcal{C}_r$; $n \sim \mathcal{CN}(0, \sigma_{\mathrm{Rx}}^2)$ is the additive white Gaussian noise with variance $\sigma_{\mathrm{Rx}}^2 = N_0 W$; N_0 is the thermal noise power spectral density; $\boldsymbol{\Phi}_{k,l}^m = \mathrm{diag}\left(\left[\phi_{k,l}^{m,1}, \ldots, \phi_{k,l}^{m,n}, \ldots, \phi_{k,l}^{m,N}\right]\right) \in \mathbb{C}^{N\times N}$ is the phase shift matrix of RIS_l assigned to $\mathrm{UE}_m \in \mathcal{C}_k$; and $\phi_{k,l}^{m,n}$ is the phase shift of the nth element of the RIS_l configured as per $\mathrm{UE}_m \in \mathcal{C}_k$. Assuming the CSI is acquired through accurate channel estimation methods [Abdallah et al.,] and $\delta_{k,l}^m = 1$, the phase shifts of RIS_b are configured as per the channel characteristics of $\mathrm{UE}_m \in \mathcal{C}_k$

$$\phi_{k,l}^{m,n} = e^{j\angle f_m} e^{-j\angle g_l^n} e^{-j\angle h_{m,l}^n}, \tag{4.5}$$

where $\angle\cdot$ denotes the phase of complex numbers. Element phases cancel the overall channel phases incurred from UE-RIS-BS cascaded channel and UE-BS direct channel.

The SIC receiver at the BS iteratively decodes $y_{r_{\mathrm{pas}}}(\boldsymbol{\Delta})$ in the descending order of received signal power. That is, the cluster member with the strongest/weakest reception power is decoded first/last such that the strongest/weakest cluster member

observes all/no intra-cluster interference from other cluster members. Correspondingly, $\widetilde{C}_r$ denotes the cluster set when the index set of the UEs is sorted in descending order according to the received signal power of the UEs. Accordingly, following from (4.4), the SINR of ith ordered $\mathrm{UE}_u \in \widetilde{C}_r$ is given by

$$\gamma^u_{r_{\mathrm{pas}}}(\mathbf{\Delta}) = \frac{p_{\mathrm{id}}\left(\sum\limits_{\forall k,l,m}\left|\mathbf{g}_l^{\mathrm{T}}\left(\mathbf{\Phi}^m_{k,l}\delta^m_{k,l}\right)\mathbf{h}^l_u\right|^2 + |f_u|^2\right)}{p_{\mathrm{id}}\left(\sum\limits_{\substack{\forall z\in\widetilde{C}_r[j>i],\\ \forall k,l,m}}\left|\mathbf{g}_l^{\mathrm{T}}\left(\mathbf{\Phi}^m_{k,l}\delta^m_{k,l}\right)\mathbf{h}^l_z\right|^2 + |f_z|^2\right) + \sigma^2_{\mathrm{Rx}}}, \tag{4.6}$$

where j corresponds to the index of the UEs with lower received signal power than ith ordered cluster member. Even though the SINR expression in (4.6) accounts for $s_u, \forall u \in C_r$ reflected from $\mathrm{RIS}_b, \forall b \in \mathcal{B}$, regardless of their assignment, the non-coherent signals reflected from RIS blocks assigned to other clusters have a negligible impact on the received signal from C_r, $y_r(\mathbf{\Delta})$. Accordingly, (4.6) can be simplified by merely considering the signal reflected from RIS_b assigned to C_r as follows:

$$\gamma^u_{r_{\mathrm{pas}}}(\mathbf{\Delta}) = \frac{p_{\mathrm{id}}\left(\sum\limits_{\forall m}\left|\mathbf{g}_b^{\mathrm{T}}\left(\mathbf{\Phi}^m_{r,b}\delta^m_{r,b}\right)\mathbf{h}^b_u\right|^2 + |f_u|^2\right)}{p_{\mathrm{id}}\left(\sum\limits_{\substack{\forall z\in\widetilde{C}_r[j>i],\\ \forall m}}\left|\mathbf{g}_b^{\mathrm{T}}\left(\mathbf{\Phi}^m_{r,b}\delta^m_{r,b}\right)\mathbf{h}^b_z\right|^2 + |f_z|^2\right) + \sigma^2_{\mathrm{Rx}}}. \tag{4.7}$$

4.1.4 Active RIS-Assisted NOMA System

We further consider the use of active RIS elements to overcome the double-fading attenuation due to the product of path losses on both links, i.e., BS-RIS and RIS-UE link and enhance signal strength. Towards this end, each active RIS element amplifies the reflected incident signal rather than only reflecting it as done in passive RIS modules. Hence, the received complex baseband signal of the proposed system

with active RIS is expressed as follows:

$$y_{r_{\text{act}}}(\mathbf{\Delta}) = \sqrt{p_{\text{id}}}\left(\sum_{\forall u \in \mathcal{C}_r}\sum_{\forall k,l,m} \underbrace{\mathbf{g}_l^{\text{T}}\mathbf{G}_{k,l}^{m}\left(\mathbf{\Phi}_{k,l}^{m}\delta_{k,l}^{m}\right)\mathbf{h}_u^{l}s_u}_{\text{UEs-RIS-BS}} + \underbrace{f_u s_u}_{\text{UEs-BS}}\right) + \sum_{\forall k,l,m}\mathbf{g}_l^{\text{T}}\left(\mathbf{\Phi}_{k,l}^{m}\delta_{k,l}^{m}\right)\mathbf{v}_{k,l}^{m} + n, \tag{4.8}$$

where $y_{r_{\text{act}}}(\mathbf{\Delta})$ is the received signal from members of $\mathcal{C}_r$ at RB_r; $\mathbf{v}_{k,l}^{m} = \text{diag}\left(\left[v_{k,l}^{m,1}, \ldots, v_{k,l}^{m,n}, \ldots, v_{k,l}^{m,N}\right]\right) \in \mathbb{C}^{N\times N}$ and $v_{k,l}^{m,n} \sim \mathcal{CN}(0, \sigma_{\text{RIS}}^2)$ is the additive white Gaussian noise at the active elements of the RISs with variance $\sigma_{\text{RIS}}^2 = N_0 W$; and $\mathbf{G}_{k,l}^{m} = \text{diag}\left(\left[\alpha_{k,l}^{m,1}, \ldots, \alpha_{k,l}^{m,n}, \ldots, \alpha_{k,l}^{m,N}\right]\right) \in \mathbb{C}^{N\times N}$ holds for the amplification factor matrix of active RISs.

Similarly for the active RIS-assisted case, the SIC receiver at the BS iteratively decodes $y_{r_{\text{act}}}(\mathbf{\Delta})$ in the descending order of the received signal power. Hence, the SINR of ith ordered $\text{UE}_u \in \widetilde{\mathcal{C}_r}$ is given as

$$\gamma_{r_{\text{act}}}^{u}(\mathbf{\Delta}) = \frac{p_{\text{id}}\left(\sum_{\forall k,l,m}\left|\mathbf{g}_l^{\text{T}}\mathbf{G}_{k,l}^{m}\left(\mathbf{\Phi}_{k,l}^{m}\delta_{k,l}^{m}\right)\mathbf{h}_u^{l}\right|^2 + |f_u|^2\right)}{p_{\text{id}}\left(\sum_{\substack{\forall z\in\widetilde{\mathcal{C}}_r[j>i],\\ \forall k,l,m}}\left|\mathbf{g}_l^{\text{T}}\left(\mathbf{\Phi}_{k,l}^{m}\delta_{k,l}^{m}\right)\mathbf{h}_z^{l}\right|^2 + |f_z|^2\right) + \sum_{\forall k,l,m}\left|\mathbf{g}_l^{\text{T}}\left(\mathbf{\Phi}_{k,l}^{m}\delta_{k,l}^{m}\right)\right|^2 + \sigma_{\text{Rx}}^2}. \tag{4.9}$$

For a similar reason as in the passive RIS-assisted scheme, (4.9) can also be simplified as

$$\gamma_{r_{\text{act}}}^{u}(\mathbf{\Delta}) = \frac{p_{\text{id}}\left(\sum_{\forall m}\left|\mathbf{g}_b^{\text{T}}\mathbf{G}_{r,b}^{m}\left(\mathbf{\Phi}_{r,b}^{m}\delta_{r,b}^{m}\right)\mathbf{h}_u^{b}\right|^2 + |f_u|^2\right)}{p_{\text{id}}\left(\sum_{\substack{\forall z\in\widetilde{\mathcal{C}}_r[j>i],\\ \forall m}}\left|\mathbf{g}_l^{\text{T}}\left(\mathbf{\Phi}_{r,b}^{m}\delta_{r,b}^{m}\right)\mathbf{h}_z^{b}\right|^2 + |f_z|^2\right) + \sum_{\forall m}\left|\mathbf{g}_l^{\text{T}}\left(\mathbf{\Phi}_{r,b}^{m}\delta_{r,b}^{m}\right)\right|^2 + \sigma_{\text{Rx}}^2}. \tag{4.10}$$

Power Limitation for the Active Components

In the proposed active RIS-assisted architecture, each reflecting element of RISs includes an active component, called fully-connected active RIS. According to [Makki

et al., 2015a], the power efficiency of these active elements can be modeled as

$$\frac{\overline{P_{\text{out},n}}}{P_{\text{cons},n}} = \eta_{\max} \left(\frac{\overline{P_{\text{out},n}}}{P_{\max}^{\text{act}}} \right)^{\varepsilon}, \tag{4.11}$$

where $P_{\text{cons},n}$, $\overline{P_{\text{out},n}}$, $\eta_{\max} \in (0, 1]$ and ε correspond to consumed power by the nth active element, the output power of the nth active element, the maximum efficiency of each active components, and a parameter depending on the amplifier hardware, respectively. The maximum output power for each active element is set to $P_{\max}^{\text{act}}$ to prevent it to operate in the non-linear region.

The proposed scheme has a power limitation for active RISs, so each can use a limited total power, P_{tot}, at most to amplify the incoming signal. Considering a fully-connected active RIS architecture and each RIS has N reflecting elements, there are also N active components for each RIS. The maximum power consumption for an ideal active element $P_{\text{cons},n}$ is obtained by reorganizing (4.11) assuming $\varepsilon = 0.5$ for more accurate modeling as follows:

$$P_{\text{cons},n} = \frac{1}{\eta_{\max}} \sqrt{\overline{P_{\text{out},n}} P_{\max}^{\text{act}}} = \frac{P_{\text{tot}}}{N}, \tag{4.12}$$

where $\eta_{\max} \in (0, 1]$ is the maximum efficiency of the active components [Persson et al., 2013, Makki et al., 2015b]. $\overline{P_{\text{out},n}}$ is the output power of the nth active component without the limitation of $P_{\max}$. Thus, $\overline{P_{\text{out},n}}$ can be extracted from (4.12) as

$$\overline{P_{\text{out},n}} = \left(\frac{P_{\text{tot}} \eta_{\max}}{N} \right)^2 P_{\max}^{\text{act}}. \tag{4.13}$$

Considering the maximum output power limitation of those active components, the optimum output power of the nth active component becomes

$$P_{\text{out},n} = \min(\overline{P_{\text{out},n}}, P_{\max}^{\text{act}}). \tag{4.14}$$

Moreover, the gain without the limitation of the maximum gain value that the nth active component can have is expressed as

$$\overline{G_{\text{opt},n}} = \frac{P_{\text{out},n}}{p_{\text{id}} |h_{u,b}^{n}|^2}. \tag{4.15}$$

Thus, the optimum gain value for the nth active component becomes

$$G_{\text{opt},n} = \min(\overline{G_{\text{opt},n}}, G_{\max}), \tag{4.16}$$

where $G_{\max}$ is the maximum gain of the active components.

4.2 Problem Definition and Solution Methodology

In this section, we first provide joint UE clustering and RIS assignment formulation of the RIS-assisted GF-NOMA system, and then provide an overview of the solution methodology.

4.2.1 Problem Definition

The joint UE clustering and RIS assignment problem that maximizes the overall network sum rate can be formulated as follows:

$$\begin{aligned}
\mathbf{P_1}: \max_{\boldsymbol{\mathcal{X}},\boldsymbol{\Delta}} \quad & \sum_{\forall r\in\mathcal{R}} \sum_{\forall u\in\mathcal{U}} W \log_2(1+\chi_r^u \gamma_r^u(\boldsymbol{\Delta})) \\
\text{s.t.} \quad & \\
\text{C}_1: \quad & \gamma_r^u \geq 2^{q_u/B} - 1, \ \forall u \in \mathcal{C}_r, \forall r \in \mathcal{R}, \\
\text{C}_2: \quad & \sum_{r\in\mathcal{R}} \chi_r^u = 1, \ \forall u \in \mathcal{U}, \\
\text{C}_3: \quad & \sum_{\forall u\in\mathcal{U}} \chi_r^u \leq K, \quad \forall r \in \mathcal{R}, \\
\text{C}_4: \quad & \delta_{r,b}^u \leq \chi_r^u, \quad \forall r \in \mathcal{R}, \forall b \in \mathcal{B}, \forall u \in \mathcal{U}, \\
\text{C}_5: \quad & \sum_{\forall u\in\mathcal{U}} \sum_{\forall b\in\mathcal{B}} \chi_r^u \delta_{r,b}^u \leq 1, \quad \forall r \in \mathcal{R}, \\
\text{C}_6: \quad & \sum_{\forall u\in\mathcal{U}} \sum_{\forall r\in\mathcal{R}} \sum_{\forall b\in\mathcal{B}} \delta_{r,b}^u \leq B, \\
\text{C}_7: \quad & \chi_r^u \in \{0,1\}, \delta_{r,b}^u \in \{0,1\}, \forall r, \forall u, \forall b,
\end{aligned} \tag{4.17}$$

where γ_r^u is the SINR of $\text{UE}_u \in \mathcal{C}_r$, $\boldsymbol{\mathcal{X}} \in \{0,1\}^{U\times R}$ is the binary UE clustering matrix with entries χ_r^u. In $\boldsymbol{P_1}$, C_1 ensures that UE_u is satisfied with the quality of service demand q_u [bps] $\forall u \in \mathcal{C}_r, \forall r \in \mathcal{R}$, C_2 assures each UE is admitted to a cluster, C_3

limits the cluster size by $K = \lceil U/R \rceil$, C_4 states that RIS_b cannot be configured as per UE_u if it is not a member of C_r, C_5 guarantees each cluster is assisted by at most one RIS block, C_6 limits the total RIS assignments by the total number of RIS blocks, and C_7 specifies the domain and bounds on optimization variables. $\mathbf{P_1}$ is a mixed-integer non-linear programming (MINLP) problem, which is non-convex due to the interference terms in the SINR expression defined in the next section. Finding an optimal solution to this NP-Hard problem is computationally prohibitive, even for moderate network size, and it necessitates a heuristic solution for real-life implementation, which is discussed next.

4.2.2 Solution Methodology

The proposed RIS-assisted GF-NOMA scheme allows UEs to access RBs at any time, requiring neither grant acquisition from the BS nor power control at the UE side. Instead, the power disparity requirement of PD-NOMA is satisfied by the UE clustering and the RIS assignment through a three-level implicit power control:

1. The first level of power control is obtained by pairing UEs with different channel gains on the same cluster/RB. Even if UEs operate at identical transmit power, the channel gain disparity introduces a reception power disparity to achieve a higher PD-NOMA gain.

2. The second level of power control is obtained by assigning a proper RIS block to a cluster. It is worth noting that RIS improves overall communication performance if it is deployed near the UE or the BS [Kilinc et al., 2021]. Therefore, RIS block assignment plays a crucial role in increasing the power reception disparity for an improved cluster sum rate.

3. The final level of power control is obtained by selecting the cluster member according to which assigned RIS is configured. Since reception power levels determine the SIC decoding order, the cluster member selection is also critical for improving the overall cluster sum rate.

Before delving into the details of the proposed UE clustering and RIS assignment solutions for the considered RIS-assisted GF-NOMA system, it is worth reminding that the optimal GB PD-NOMA scheme requires UEs with stronger channels to transmit at the higher powers to maximize the UL-NOMA cluster sum rate [Celik, 2021]. However, this approach is not fair in energy consumption and may result in reduced network lifetime, which is paramount for low-power mMTC. Alternatively, the proposed approaches improve network lifetime by requiring all UEs to transmit at identical power fairly and constitutes the required power disparity through iterative UE clustering and RIS assignments introduced in Section 4.3.

4.3 UE Clustering and RIS Assignment Algorithms

In this section, we introduce the proposed UE clustering and RIS assignment schemes. Following cluster initialization, the proposed iterative approach admits a single UE to each cluster at each iteration until all UEs are admitted to a cluster. To this aim, the admissions are determined based on two different algorithms. Algorithm 1 jointly assigns UEs and RISs to clusters and executes a 3D-AA that yields the maximum network sum rate; therefore, it is called joint UE clustering and RIS assignment algorithm. Algorithm 2 first assigns UEs to clusters by using linear sum assignment (LSA). After that, it assigns RIS blocks to formed clusters by using LSA again. Since the second assignment first forms clusters and then makes RIS assignments, it follows a two-step process, unlike Algorithm 1, which is called consecutive UE clustering and RIS assignment algorithm.

4.3.1 Joint 3D UE Clustering and RIS Assignment Algorithm

Algorithm 1 follows an iterative joint 3D assignment approach. At each iteration, a 3D cost matrix is generated whose elements represent cluster rates for each combination of UE admission and RIS assignment status. UEs and RISs are then jointly assigned to clusters using a 3D-AA.

Algorithm 1 starts with receiving sounding reference signals (SRS), which is a Zadoff-Chu sequence transmitted by each UE separately from the Physical UL

Algorithm 1 : Joint UE Clustering and RIS Assignment

Input: $\mathcal{R}$, $\mathcal{U}$, $\mathcal{B}$, P
$\mathbf{h}_u^b / \mathbf{g}_b / f_u \leftarrow$ *Acquire CSI from SRS sent by* $UE_u, \forall u \in \mathcal{U}, \forall b \in \mathcal{B}$
$C \leftarrow R$ *// Determine number of clusters*
$K \leftarrow \lceil \frac{U}{R} \rceil$ *// Determine maximum cluster size*
$\tilde{\mathcal{U}} \leftarrow$ SortDescend$(\mathfrak{RSS}, \forall u)$ *// UE ordering based on RSS of SRS signals*
$C_r \leftarrow \tilde{\mathcal{U}}\{r\}, r \in [1, \ldots, R]$ *// Initialize clusters*
$\chi_r^u \leftarrow 1, u \in C_r$ *//Initialize UE clustering matrix*
for $k = 1 : K-1$ **do** *// Iterative UE admission and RIS Assignment starts*
  $\mathcal{A}_k \leftarrow \tilde{\mathcal{U}} - \bigcup_{r=1}^{R} C_r$ *// Initialize admission awaiting UEs*
  $\boldsymbol{Q_k}, \boldsymbol{I_k} \leftarrow$ Cost Matrix$(\boldsymbol{C}_r, \mathcal{A}_k, \mathcal{B})$ *// Generating cost matrix*
  $\boldsymbol{Y}_k \leftarrow$ 3D-Axial Assignment$(\boldsymbol{Q_k}, \mathcal{A}_k)$
  $C_r \leftarrow C_r \bigcup \mathcal{A}_k\{u\}, y_{r,b}^u = 1, \forall (r, u, b)$ *// Update clusters*
  $\chi_r^u \leftarrow 1, u \in C_r$ *// Update UE clustering matrix*
  $\delta_{r,b}^{u'} \leftarrow 1$ iff $u' = \iota_{r,b}^u$, $u \in C_r, \forall (r, b)$ *//Update RIS assignment matrix*
end for
return $\boldsymbol{\chi}$, $\boldsymbol{\Delta}$

procedure Cost Matrix$(\boldsymbol{C}_r, \mathcal{A}_k, \mathcal{B})$
  $\boldsymbol{Q}, \boldsymbol{I} \leftarrow \mathbf{0}^{R \times A \times B}$ *// Initialize* $\boldsymbol{Q}$ *and* $\boldsymbol{I}$ *to matrix of zeros*
  for $r = 1 : \mathcal{R}$ **do**
    for $b = 1 : B$ **do**
      for $u = 1 : A$ **do**
        $\mathcal{T}_r \leftarrow C_r \bigcup \mathcal{A}_k\{u\}$ *// Temp. admit* u^{th} *UE of* $\mathcal{A}_k$ *to* C_r
        for $j \in T_r$ **do**
          $\boldsymbol{\Phi}_{r,b}^j \leftarrow$ Align RIS_b to $\text{UE}_{\mathcal{T}_r\{j\}}$ as per (4.5)
          $\gamma_r^j \leftarrow$ Obtain SINR as per (4.7)/(4.10) for pas./act. RIS
          $\eta_j^\star \leftarrow \sum_{j \in \mathcal{T}_r} W \log_2(1 + \gamma_r^j)$
        end for
        $q_{r,b}^u \leftarrow \max(\eta_j^\star, j \in \mathcal{T}_r)$ *// Update cost matrix entries*
        $\iota_{r,b}^u \leftarrow \text{argmax}(\eta_j^\star, j \in \mathcal{T}_r)$ *// Update* $\boldsymbol{I}$ *entries*
      end for
    end for
  end for
return $\boldsymbol{Q}, \boldsymbol{I}$
end procedure

procedure 3D-Axial Assignment$(\boldsymbol{Q}, \mathcal{A}_k)$
  $\overset{\star}{\boldsymbol{Y}} \leftarrow \max_{\boldsymbol{Y}} \ \sum_{r \in \mathcal{R}} \sum_{b \in \mathcal{B}} \sum_{u \in \mathcal{U}} q_{r,b}^u y_{r,b}^u$
    s.t. $\sum_{r \in \mathcal{R}} \sum_{b \in \mathcal{B}} y_{r,b}^u = 1, \forall u \in \mathcal{A}_k$
    $\sum_{r \in \mathcal{R}} \sum_{u \in \mathcal{U}} y_{r,b}^u = 1, \forall b \in \mathcal{B}$
    $\sum_{b \in \mathcal{R}} \sum_{u \in \mathcal{U}} y_{r,b}^u = 1, \forall r \in \mathcal{R}$
return $\overset{\star}{\boldsymbol{Y}}$
end procedure

shared channel (PUSCH) and physical UL control channel (PUCCH). UEs can transmit SRS on any subcarriers in the last symbol of an UL subframe regardless of subcarriers assignments. We especially focus on time-division duplexing (TDD) mode for the sake of channel reciprocity such that SRS may also be sent in the last two symbols of the special subframe if UL pilot time slot (UpPTS) is configured to be in the long format. The SRS is imperative to estimate cascaded and direct channels [Abdallah et al.,] to determine RIS assignment and configure phase shift matrices accordingly. Notice that the CSI acquisition is an inherent part of any communication system and not specific to the proposed approach. After the cluster size is determined based on the available number of RBs in Line 3, the maximum cluster size is determined in Line 4 based on the UE density. For the sake of cluster initialization, the UEs are sorted in the descending order of received signal strength of SRS signals in Line 5. Then, the clusters are initialized by admitting the first R UEs into C clusters in Line 6. Then, the iterative UE admission and RIS assignment starts in Line 8, in each iteration one more UE is admitted to each cluster. Therefore, the first line of the for loop, Line 9, updates the set of UEs awaiting cluster admission, which is denoted by $\mathcal{A}_k$.

To execute 3D-AA, Line 10 calls cost matrix generation procedure given between Line 17 and Line 34, where cost matrix $\boldsymbol{Q} \in \mathbb{R}^{R\times A\times B}$ and temporary RIS alignment matrix $\boldsymbol{I} \in \mathbb{N}^{R\times A\times B}$ are formed over three nested for loops. In Line 22, the u-th element of admission awaiting UE set is temporarily admitted to $\mathcal{C}_r$. Then, the most inner loop between Line 23 and Line 27 determines the cluster member giving the maximum cluster sum rate if RIS_b is aligned as per its channel conditions. To this aim, Line 24 adjusts the phase shift matrix of RIS_b to $\text{UE}_{\mathcal{T}_r\{j\}}$, Line 25 calculates the cluster members' SINR based on adjusted the phase shift matrix as per (4.7)/(4.10) for passive/active RIS, and finally Line 26 records the cluster sum rate of $\mathcal{T}_r$ if RIS_b is aligned to its j-th member, $\eta_j^\star$. Accordingly, the cost matrix element $q_{r,u}^b$ is updated in Line 28 based on the UE cluster member giving the highest possible cluster rate if the phase shift matrix of RIS_b is aligned to itself, whose index matrix (representing the UE index) is also stored in a temporary RIS alignment matrix in Line 29.

Following the generation of the cost-matrix, Line 11 calls 3D-Axial Assign-

MENT to find joint UE clustering and RIS assignment at k-th iteration. For instance, when 3D-AA returns $y^5_{3,4} = 1$, it means that: 1) $\text{UE}_{\mathcal{A}_k\{5\}}$ is admitted to $\mathcal{C}_3$, 2) RIS_4 is assigned to $\mathcal{C}_3$, and 3) phase shift matrix of RIS_4 is aligned to assisted UE whose UE index stored in $u' = \iota^5_{3,4}$. Thereafter, the cluster members are updated as per the outcome of 3D-AA in Line 12, which is followed by update of UE clustering matrix $\boldsymbol{\mathcal{X}}$ and RIS assignment matrix $\boldsymbol{\Delta}$ in Line 13 and 14, respectively. The final UE clustering and RIS assignment matrices are returned at the end of $(K-1)$-th iteration. Notice in Line 14 that the phase alignment is obtained from the RIS alignment matrix $\boldsymbol{I}$ returned by the COST MATRIX procedure.

The time complexity of the proposed solution is mainly driven by COST MATRIX and 3D-AXIAL ASSIGNMENT procedures. The complexity of cost matrix computation is $\mathcal{O}\left(\sum_{k=1}^{K-1} RA_kB\right)$. Moreover, the 3D-AA is known to be an NP-Hard problem, whose matching theory-based approximate solutions can obtain results for a square cost matrix with complexity $\mathcal{O}\left(3MV^3\right)$ where M is the number of relaxations and V is the largest dimension of the cost matrix [Pattipati et al., 1992]. Hence, after $K-1$ iterations, the time complexity of the considered 3D-AA becomes $\mathcal{O}\left(3M\sum_{k=1}^{K-1}(V_k)^3\right)$, where $V_k = \max(R, A_k, B)$. Since the latter is more dominant, the overall complexity can be approximated as $\sim \mathcal{O}\left(3M\sum_{k=1}^{K-1} RA_kB + (V_k)^3\right)$.

4.3.2 Consecutive 2D UE Clustering and RIS Assignment Algorithm

Algorithm 2 proposes a faster and consecutive UE clustering and RIS assignment algorithm that achieves almost the same performance as Algorithm 1. Algorithm 2 mainly follows a similar iterative clustering approach but instead of jointly assigning UEs and RIS blocks to cluster sets, it first assigns UEs to the clusters and then assigns RISs to previously formed clusters. Lines 2-6 performs setting obtaining CSI information, determining number of clusters and maximum cluster size, initializing clusters respectively, as in Algorithm 1.

The iterative UE admission starts in Line 8, in each iteration one more UE is admitted to each cluster. Therefore, the first line of the for loop, Line 9, updates the set of UEs awaiting cluster admission, which is denoted by $\mathcal{A}_k$. The iterative

Algorithm 2 : Consecutive UE Clustering and RIS Assignment

Input: $\mathcal{R}$, $\mathcal{U}$, $\mathcal{B}$, P
$\mathbf{h}_u^b/\mathbf{g}_b/f_u \leftarrow$ *Acquire CSI from SRS sent by* $UE_u, \forall u \in \mathcal{U}, \forall b \in \mathcal{B}$
$C \leftarrow R$ *// Determine number of clusters*
$K \leftarrow \lceil \frac{U}{R} \rceil$ *// Determine maximum cluster size*
$\tilde{\mathcal{U}} \leftarrow$ SortDescend$(\mathfrak{RSS}, \forall u)$ *// UE ordering based on RSS of SRS signals*
$\mathcal{C}_r \leftarrow \tilde{\mathcal{U}}\{r\}, r \in [1, \ldots, R]$ *// Initialize clusters*
$\chi_r^u \leftarrow 1, u \in \mathcal{C}_r$ *//Initialize UE clustering matrix*
for k=1 : K−1 **do** *// Iterative UE admission and RIS Assignment starts*
  $\mathcal{A}_k \leftarrow \tilde{\mathcal{U}} - \bigcup_{r=1}^{R} \mathcal{C}_r$ *// Initialize admission awaiting UEs*
  $\boldsymbol{Q_k} \leftarrow$ Cost Matrix UE$(\boldsymbol{C}_r, \mathcal{A}_k)$ *// CM for user clustering*
  $\boldsymbol{Y}_k \leftarrow$ 2D-Axial Assignment$(\boldsymbol{Q_k})$
  $\mathcal{C}_r \leftarrow \mathcal{C}_r \bigcup \mathcal{A}_k\{u\}, y_r^u = 1, \forall (r, u)$ *// Update clusters*
  $\chi_r^u \leftarrow 1, u \in \mathcal{C}_r$ *// Update UE clustering matrix*
end for
return $\boldsymbol{\chi}$
$\boldsymbol{Q_m}, \boldsymbol{I_m} \leftarrow$ Cost Matrix RIS$(\boldsymbol{C}_r, \mathcal{B})$ *// CM for RIS assignment*
$\boldsymbol{Y}_m \leftarrow$ 2D-Axial Assignment$(\boldsymbol{Q_m})$
$\delta_{r,b}^{u'} \leftarrow 1$ iff $u' = \iota_r^b, y_r^b = 1$, $u \in \mathcal{C}_r, \forall (r, b)$ *//Update RIS assignment matrix*
return $\boldsymbol{\Delta}$

procedure Cost Matrix UE$(\boldsymbol{C}_r, \mathcal{A}_k)$
  $\boldsymbol{Q}, \boldsymbol{I} \leftarrow \mathbf{0}^{R \times A}$ *// Initialize* $\boldsymbol{Q}$ *and* $\boldsymbol{I}$ *to matrix of zeros*
  for $r = 1 : \mathcal{R}$ **do**
    for $u = 1 : A$ **do**
      $\mathcal{T}_r \leftarrow \mathcal{C}_r \bigcup \mathcal{A}_k\{u\}$ *// Temp. admit* u^{th} *UE of* $\mathcal{A}_k$ *to* $\mathcal{C}_r$
      $\gamma_r^j \leftarrow$ Obtain SINR of UE_j, $\forall j \in \mathcal{T}_r$
      $q_r^u \leftarrow \sum_{j \in \mathcal{T}_r} W \log_2(1 + \gamma_r^j)$
    end for
  end for
return $\boldsymbol{Q}$

end procedure

procedure Cost Matrix RIS$(\boldsymbol{C}_r, \mathcal{B})$
  $\boldsymbol{Q}, \boldsymbol{I} \leftarrow \mathbf{0}^{R \times B}$ *// Initialize* $\boldsymbol{Q}$ *and* $\boldsymbol{I}$ *to matrix of zeros*
  for $r = 1 : \mathcal{R}$ **do**
    for $b = 1 : B$ **do**
      for $j \in \mathcal{C}_r$ **do**
        $\boldsymbol{\Phi}_{r,b}^j \leftarrow$ Align RIS_b to $\text{UE}_{\mathcal{C}_r\{j\}}$ as per (4.5)
        $\gamma_r^j \leftarrow$ Obtain SINR as per (4.7)/(4.10) for pas./act. RIS
        $\eta_j^\star \leftarrow \sum_{j \in \mathcal{T}_r} W \log_2(1 + \gamma_r^j)$
      end for
      $q_r^b \leftarrow \max(\eta_j^\star, j \in \mathcal{C}_r)$ *// Update cost matrix entries*
      $\iota_r^b \leftarrow \text{argmax}(\eta_j^\star, j \in \mathcal{C}_r)$ *// Update* $\boldsymbol{I}$ *entries*
    end for
  end for
return $\boldsymbol{Q}, \boldsymbol{I}$
end procedure

procedure 2D-Axial Assignment$(\boldsymbol{Q})$
  $\hat{\boldsymbol{Y}} \leftarrow \max_{\boldsymbol{Y}} \ \sum_{r \in \mathcal{R}} \sum_{z \in \mathcal{Z}} q_r^z y_r^z$
    s.t. $\sum_{r \in \mathcal{R}} y_r^z = 1, \forall z \in \mathcal{Z}$
    $\sum_{z \in \mathcal{Z}} y_r^z = 1, \forall r \in \mathcal{R}$
    $z \in \{u, b\}, \mathcal{Z} \in \{\mathcal{U}, \mathcal{B}\}$
return $\hat{\boldsymbol{Y}}$
end procedure

algorithm now only admits UEs to the clusters and starts in Line 8. In line 9 the set $\mathcal{A}_k$ is updated that denotes the admission awaiting UEs. In each iteration one more UE is admitted to each cluster from the set $\mathcal{A}_k$. Line 10 calls the cost matrix function for UE admission. The 2D Cost matrix $\boldsymbol{Q}_k \in \mathbb{R}^{R \times A}$ is generated between the Lines 20-31 over two nested loops. Line 24 admits the uth UE from the set $\mathcal{A}_k$ to $\mathcal{C}_r$ and forms a temporary cluster denoted by $\mathcal{T}_r$. The UE SINRs are calculated in Line 25 and the temporary cluster rate is calculated by summing the rates of UEs in $\mathcal{T}_r$. The cost matrix element q_r^u in Line 26 stands for the cluster rate if uth UE from the set $\mathcal{A}_k$ is assigned to $\mathcal{C}_r$. Notice that the UE assignment merely depends on channel gain disparity among the UEs and does not consider RIS assistance and phase shift alignment.

The UE admission is performed according to LSA executed in Line 11 to find the assignment maximizing the network sum rate by using the generated cost matrix at kth iteration. For instance, when LSA returns $y_3^5 = 1 \in \boldsymbol{Y}_k$, it means that $\text{UE}_{\mathcal{A}_k\{5\}}$ is admitted to $\mathcal{C}_3$. In the final step, UE clustering matrix $\boldsymbol{\mathcal{X}}$ is updated. After finalizing the UE admission and forming clusters, RIS blocks needs to be assigned to generated clusters and assist specific UEs in each cluster to maximize the cluster rate. Line 16 calls the cost matrix function for RIS assignment and phase alignment purposes. The cost matrix $\boldsymbol{Q}_m \in \mathbb{R}^{R \times B}$ and a temporary RIS alignment matrix $\boldsymbol{I}_m \in \mathbb{N}^{R \times B}$ are formed over three nested for loops in procedure explained between lines 32-46. The first two loops in lines 34 and 35 assign $\text{RIS}_b \in \mathcal{B}$ to $\mathcal{C}_r$. The most inner loop finds the UE that maximizes the cluster sum rate when the corresponding RIS block's phase shifts are aligned to itself. Line 37 aligns the phase of the RIS_b to UE $j \in \mathcal{C}_r$. Following SINRs are calculated by considering the phase configuration of the RIS block in Line 38. Line 39 records the cluster sum rate if RIS_b is assigned to UE j in $\mathcal{C}_r$. In consequence, the cost matrix element q_r^u in Line 42 is obtained by considering the cluster member yielding the largest cluster rate when assisted with RIS_b and its UE index is stored in ι_r^b. Finally, LSA procedure is called again in Line 17 to find the RIS assignment and alignment at once. For instance, if LSA returns $y_2^4 = 1 \in \boldsymbol{Y}_k$ for user clustering, it means that RIS_4 is assigned to $\mathcal{C}_2$. Likewise, if LSA returns $y_2^4 = 1 \in \boldsymbol{Y}_m$ for RIS assignment/alignment, it means that the phase configuration

of the RIS_4 is aligned for $\text{UE}_{u'}$ whose UE index is stored in ι_2^4. Thereafter, the elements of the RIS assignment matrix $\delta_{r,b}^{u'}$ is updated in Line 18 and returned the final assignment matrix $\mathbf{\Delta}$ in 19.

The time complexity of the consecutive approach is mainly driven by Cost Matrix and LSA procedures. The complexity of cost matrix computation for UE clustering and RIS assignment are given by $\mathcal{O}\left(\sum_{k=1}^{K-1} RA_k\right)$ and $\mathcal{O}\left(RB\right)$, respectively. Considering the well known cubic complexity of LSA solutions, the overall complexity can be obtained as $\mathcal{O}\left(\sum_{k=1}^{K-1} RA_k + (\max(R, A_k))^3\right)$ and $\mathcal{O}\left(RB + (\max(R, B))^3\right)$, which constitutes the entire complexity of Algorithm 2 together.

4.4 Numerical Results

In this section, we provide numerical results for the proposed schemes and compare their performances with three benchmark schemes for different system parameters. Achievable rates and fairness indexes for different schemes are presented by computer simulations. Although we consider the SINR expressions in (4.7)/(4.10) for passive/active RIS assignment in both algorithms, we consider the general SINR expression in (4.6)/(4.9) while obtaining the numerical results, so that the reflections from non-coherent RIS blocks are considered as well. We consider the default system parameters summarized in Table 4.1, unless stated explicitly otherwise.

4.4.1 Benchmark Schemes

For evaluation of the RIS-Assisted GF-NOMA scheme, this section presents three benchmark schemes [Celik, 2021]:

1. The optimum PD-NOMA (OPT PD-NOMA) where UEs compute optimal power control based on the readily available CSI, and the maximum and minimum transmit power of UEs are $P_{\max}$ and $P_{\min}$, respectively. Throughout the simulations, optimal power weights are obtained by geometric programming solver of the CVX disciplinized convex optimization toolbox [Grant and Boyd, 2014].

Table 4.1: Table of the simulation parameters

Param.	Def.	Value	Param.	Def.	Value
U	# UEs	75	N	# Reflecting elements	256
R	# RBs	25	q_u	Quality of service demand of UEu	0.1 Mbps
M	# RISs	25	f_c	Carrier frequency	5 GHz
G	# sub-blocks	1	p_{id}	Identical power	21 dBm
C	# clusters	25	$P_{\max}$	Maximum transmit power of the UEs	23 dBm
N_0	Thermal noise power spectral density	−174 dBm	$P_{\min}$	Minimum transmit power of the UEs	−40 dBm
D	Cell radius	250 m	$P_{\max}^{\text{act}}$	Maximum output power for each active element	21 dBm
D_{in}	RIS area inner radius	15 m	P_{tot}	Maximum power consumed by an active RIS	1 W
D_{out}	RIS area outer radius	50 m	$G_{\max}$	Maximum gain of the active components	20 dB
W	Resource block bandwith	180 kHz			

2. Multi-level GF-NOMA (MGF-NOMA) scheme partitions the set of UEs into $R = C$ groups based on their channel gains and divides power control range ($[p_{max} = 23, p_{min} - 40]$ dBm) into $R = C$ levels. MGF-NOMA requires UE partitions with higher channel gain to transmit at higher power levels. For instance, the UE partition consisting of UEs with the highest/lowest channel gains are required to transmit at the highest/lowest power levels.

3. Single level GF-NOMA (SGF-NOMA) scheme requires all UEs transmit at an identical transmit power, p_{id}.

We refer interested readers to [Celik, 2021] for a more detailed explanation of the benchmark schemes. For the sake of a fair comparison, the benchmark schemes follow the clustering approach presented in Algorithm 2. Additionally, for the same reason, the proposed schemes uses $p_{\text{id}} = 21$ dBm for all UEs, which is the average transmit power of UEs for OPT PD-NOMA. Noting that benchmark schemes do not benefit from RIS, the main difference between compared schemes is the underlying power control approach.

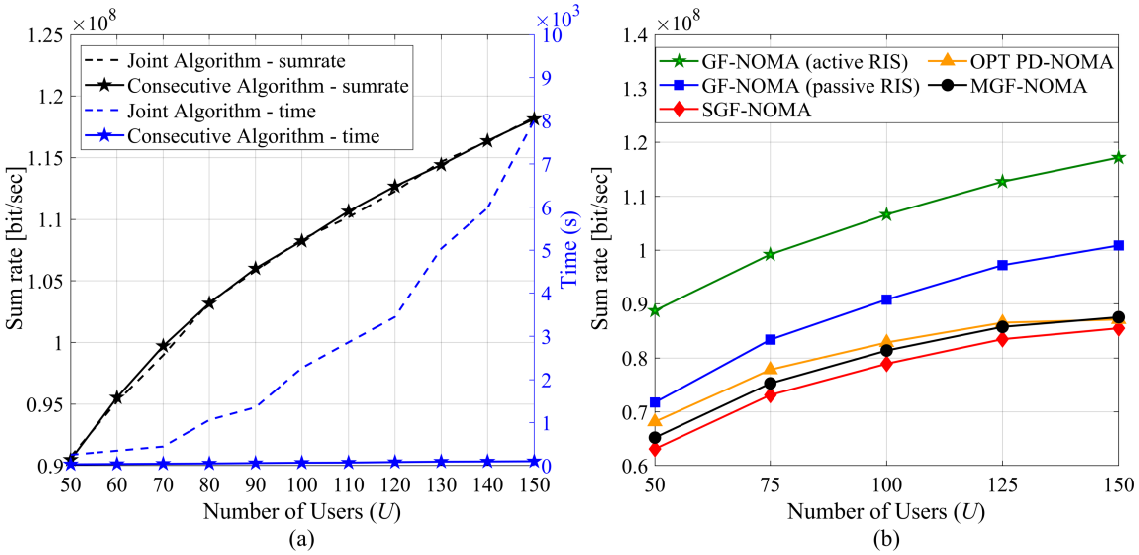

Figure 4.2: (a) Sum rate and complexity of the proposed algorithms, and (b) sum rate of the proposed schemes

4.4.2 Impact of UE Density on Sumrate and Time Complexity

The number of UEs in the network is a crucial metric affecting both network performance and the complexity of the NOMA schemes. Fig. 4.2 shows run time complexity and network achievable network sum rate for varying U. As seen in Fig. 4.2(a), the consecutive algorithm returns result up to 80 times faster than the joint Algorithm 1 while achieving almost the same network sum rate performance as shown in 4.2(b). Such a great run time complexity difference is mainly due to the time spent generating the 3D cost matrix for Algorithm 1, which increases as U increases. Since the consecutive approach provides almost the same performance with much-reduced running times, the rest of the simulations are carried out with Algorithm 2.

As seen in Fig. 4.2(b), the sum rate of the proposed scheme increases with U because the number of UEs operating in a single RB increases, resulting in more efficient spectrum usage. The proposed scheme with passive RISs performs up to 15%, 15%, and 18% better than OPT PD-NOMA, MGF-NOMA, and SGF-NOMA schemes when $U = 150$, respectively. When active RIS architecture is employed, the

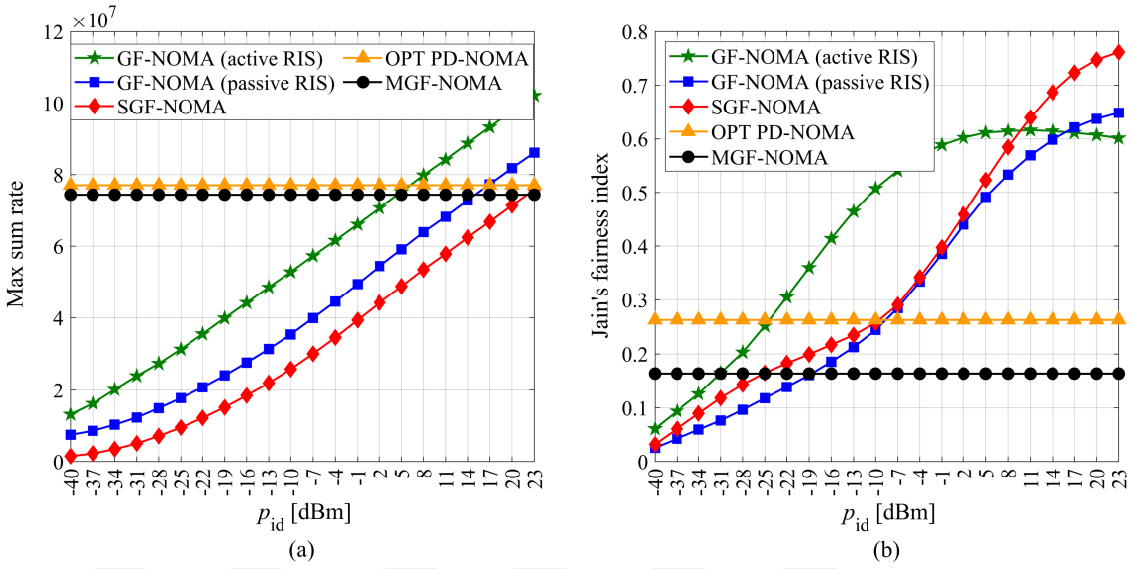

Figure 4.3: Sum rate and Jain's fairness index for varying p_{id} for the proposed and benchmark schemes

proposed scheme performs up to 34%, 34%, and 37% better than OPT PD-NOMA, MGF-NOMA, and SGF-NOMA, respectively. Thus, active RISs provide 19% better performance than passive RISs. We note that the increase in the cluster size does not negatively affect the network performance. The proposed scheme performs better on denser networks, where $U = 150$ and the number of UEs per cluster is 6 and outperforms the benchmark schemes. The performance of the benchmark schemes starts to saturate after $U = 150$ while the proposed scheme continues to show an upwards trend.

4.4.3 The Impact of Identical Tx Power on Fairness

The network sum rate for varying identical transmit power levels, p_{id}, is presented in Fig. 4.3(a). As the p_{id} varies for SGF-NOMA and active/passive RIS-assisted GF-NOMA, transmit power levels are fixed in MGF-NOMA, and the average transmit power between UEs is obtained as 21 dBm for adaptively regulated OPT PD-NOMA via Monte Carlo simulations. While the SGF-NOMA achieves the same performance as MGF-NOMA and OPT GF-NOMA at the maximum transmit power level, the

RIS-assisted schemes require less power at the UE side, resulting in more energy-efficient transmission. The passive RIS-assisted scheme requires 4 dB, and the active RIS-assisted scheme requires 16 dB less transmit power to achieve the same performance as OPT PD-NOMA and MGF-NOMA. The evaluation of the fairness in terms of the energy efficiencies of the UEs sharing the same cluster is presented in Fig. 4.3(b). The Jain's fairness index is obtained for each scheme as follows:

$$\mathcal{J} = \frac{\left(\sum_{\forall u \in C_r} \eta_u\right)^2}{K\left(\sum_{\forall u \in C_r} \eta_u\right)} \tag{4.18}$$

where $\eta_u = R_u/P_{\mathrm{t}}^u$, R_u, P_{t}^u are the bit per joule energy efficiency, the achievable rate, and transmit power of the UE_u, respectively. Since UEs transmit at identical power levels, the SGF-NOMA and RIS-assisted GF-NOMA schemes present higher fairness. While the SGF-NOMA and passive RIS-assisted GF-NOMA perform close fairness results, the active RIS-assisted scheme is the fairest scheme up to 8 dBm transmit power. Assisting low-rate UEs with active RIS yields a more fair energy usage. However, as the transmit power of the UEs increases, achievable rates of the assisted UEs become dominant, resulting in poorer fairness compared to the SGF-NOMA. Looking at Fig. 4.3, it can be concluded that RIS-assisted GF-NOMA schemes maintain fairness among UEs while providing enhanced capacity and sometimes even more fair structure.

Network sum rate for varying D_{out} and R are presented in Fig. 4.4(a) and 4.4(b), respectively. As seen in Fig. 4.4(a), the locations of the RISs substantially affect the system performance. It is a well-known fact that a basic RIS-assisted system exhibits its maximum performance when the RIS is located near the system's terminals. Similarly, the proposed design performs best when the RISs are close to the BS or UEs. The results show that deploying RISs near the BS performs better than the uniform deployment of RIS across the cell area. This is mainly because we cannot guarantee that the RISs will be placed close to the UEs since UEs are also randomly distributed. The proposed scheme performs 8%, 12%, and 15% better than OPT PD-NOMA, MGF-NOMA, and SGF-NOMA schemes, respectively, when $D_{\mathrm{out}} = 80$

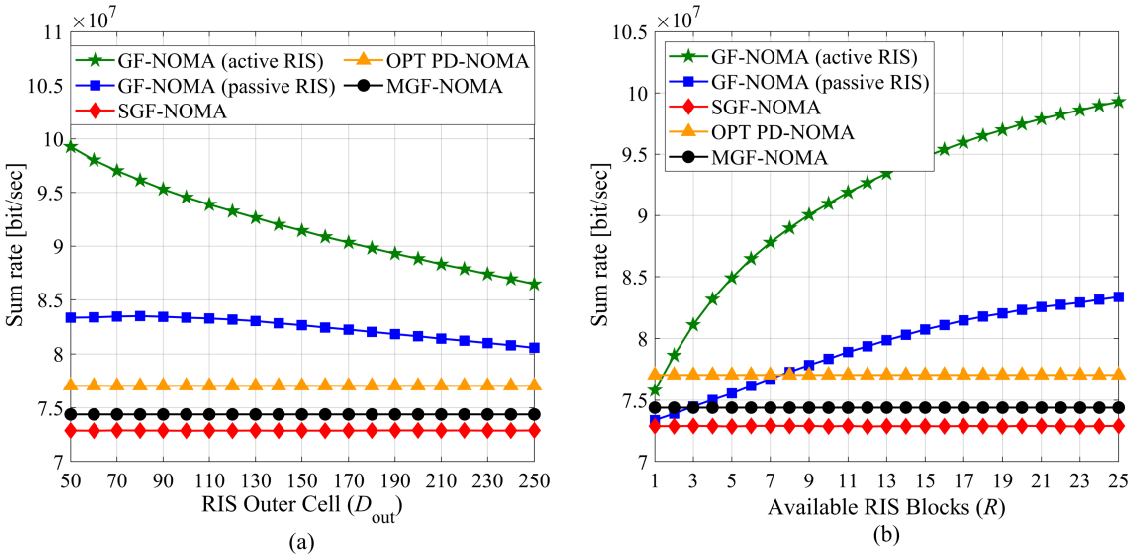

Figure 4.4: Sum rate of the network for different varying RIS metrics: (a) D_{out} and (b)R.

m with passive RISs. When active RISs are used, the proposed scheme performs 25%, 30%, and 32% better than OPT PD-NOMA, MGF-NOMA, and SGF-NOMA, respectively. Thus, the active RIS scheme gives around 18% higher performance than the passive RIS scheme. As D_{out} increases, the network sum rate decreases because the RISs gradually become distant from the BS and most of the UEs. Nevertheless, the proposed scheme still performs 5%, 8%, and 11% better than OPT PD-NOMA, MGF-NOMA, and SGF-NOMA schemes, respectively, when D_{out} = 250 m with passive RISs. The enhancement percentages are 12%, 16%, and 19% for the case where active RISs are used, respectively. We previously mentioned that an RIS could assist the other UEs in different clusters, even if its phases are aligned with the dedicated UE. This condition also helps further improve the network sum rate when the RIS is close to the BS.

As observed in Fig. 4.4(b), the network performance increases with R because more spectrum are available and more cluster becomes able to use an RIS. Using passive RISs for the proposed algorithm gives 8%, 12%, and 14% better performances than OPT PD-NOMA, MGF-NOMA, and SGF-NOMA, respectively. Likewise, it enhances the network sum rate by 29%, 33%, and 36% for OPT PD-NOMA, MGF-

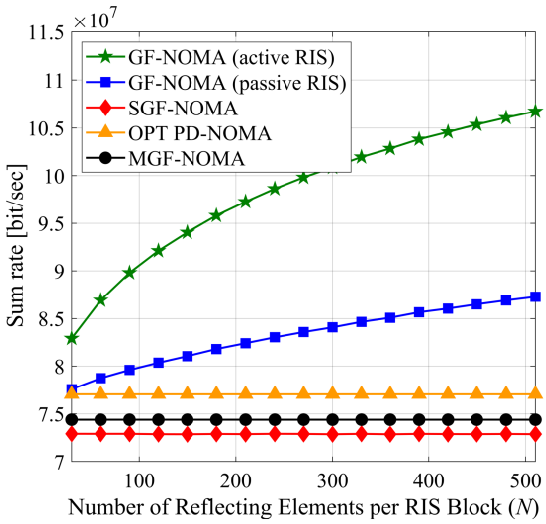

Figure 4.5: Sum rate of the network for different varying N.

NOMA, and SGF-NOMA, respectively, when active RISs are used. Additionally, using active RISs results in 19% better performance than using passive ones. Here, we note that using eight passive RISs gives nearly the same sum rate as using two active RISs.

Finally, Fig. 4.5 represents the sum rate of the network for varying N. The figure shows that the sum rate increases with N, similar to the case in Fig. 4.4(b). When passive RISs are used, the network's performance is enhanced by 13%, 17%, and 20% for OPT PD-NOMA, MGF-NOMA, and SGF-NOMA, respectively. For the other case that uses active RISs instead of the passive ones, the sum rate of the network is increased by 39%, 44% and 47% for OPT PD-NOMA, MGF-NOMA, and SGF-NOMA, respectively. In addition, a 22% increase in the network performance can be achieved by using active RISs instead of passive RISs. We emphasize that using $N = 30$ gives nearly the same sum rate as OPT PD-NOMA, meaning that we can achieve the same performance by using RISs with a very small number of reflecting elements. This amount is much lower when the active ones are used.

Chapter 5

CONCLUSION

In this thesis, we have proposed an amplifying RIS design that utilizes a single PA. The differences and advantages of the proposed design have been clearly pointed out compared to the conventional passive RIS design. We have presented its signal model for the amplifying RIS systems, and optimized the amplifier gain and the phase response of RIS_1 and RIS_2 to maximize the achievable rate. Ultimately, active RIS-assisted systems provide higher communication capacity and better error rate performance than the passive RIS-assisted systems. In addition, they enable the flexibility to place the amplifying RIS anywhere in between Tx and Rx as it greatly reduces the effect of double path loss, unlike passive RIS that should be placed closer to Tx or Rx. On top of that, active RIS-assisted systems are more energy efficient, although they consume more power. Extending our design to MIMO systems introduces complex optimization problems such as the joint optimization of transmit precoding, phases of the reflecting elements, and gain of the PA needed. Potentially, deep learning and alternating optimization algorithms can be used to deal with these problems. Future works may also include joint uplink and downlink communication, the optimization and extension of this system to MIMO systems, as well as real-world experimental results.

This thesis has also proposed two iterative clustering algorithms with 3D and 2D assignment approaches for an RIS-assisted GF-NOMA system. The performances of both active and passive RIS have been considered to boost the capacity of a GF-NOMA system. Through the proposed algorithms, the network can leverage RIS assistance to create received power disparity among NOMA UEs without the need for complex power control. Also, Algorithm 2 has been found to be faster and superior to Algorithm 1 in terms of complexity. Moreover, assisting the system with RISs results in better SIC due to the power disparity introduced from the presence of

the RISs, leading to improved achievable rates compared with the conventional GF-NOMA with no RIS assistance. Furthermore, it has also been shown that active RIS-assisted systems are superior to passive RIS-assisted systems in terms of maximizing the overall network sum rate and fairness among UEs, as they contain PAs in each element and enable us to exhibit a better SIC. Additionally, GF-NOMA schemes with identical transmit power have been shown to provide more fairness among UEs in a cluster in terms of energy efficiency. Future works can consider assisting not only one UE but multiple UEs in a cluster and the multiple cell scenarios where UEs are also jointly assigned to the BSs, which can come up with some complex optimization problems.

BIBLIOGRAPHY

[3GP, 2019] (2019). 3GPP TR 38.901 V16.1.0 - Study on channel model for frequencies from 0.5 to 100 GHz.

[Abari et al., 2017] Abari, O., Bharadia, D., Duffield, A., and Katabi, D. (2017). Enabling high-quality untethered virtual reality. In *14th USENIX Symp. on Netw. Syst. Design Implement.*, pages 531–544.

[Abbas et al., 2019] Abbas, R., Shirvanimoghaddam, M., Li, Y., and Vucetic, B. (2019). A novel analytical framework for massive grant-free noma. *IEEE Trans. Commun.*, 67(3):2436–2449.

[Abdallah et al.,] Abdallah, A., Celik, A., Mansour, M. M., and Eltawil, A. M. Deep learning-based channel estimation for wideband RIS-aided mmWave MIMO system with beam squint. Accepted to appear in ICC 2022.

[Alamzadeh et al., 2021] Alamzadeh, I., Alexandropoulos, G. C., Shlezinger, N., and Imani, M. F. (2021). A reconfigurable intelligent surface with integrated sensing capability. *Sci. Rep.*, 11(20737):1–10.

[Aldababsa et al., 2021] Aldababsa, M., Khaleel, A., and Basar, E. (2021). Simultaneous transmitting and reflecting intelligent surfaces-empowered NOMA networks. [Online] https://arxiv.org/abs/2110.05311.

[Aldababsa et al., 2022] Aldababsa, M., Khaleel, A., and Basar, E. (2022). STAR-RIS-NOMA networks: An error performance perspective. *IEEE Commun. Lett.*, pages 1–1. (early access).

[Alexandropoulos et al., 2020] Alexandropoulos, G. C., Islam, M. A., and Smida, B. (2020). Full duplex hybrid A/D beamforming with reduced complexity multi-

tap analog cancellation. In *Proc. IEEE 21st Int. Workshop Signal Process. Adv. Wireless Commun. (SPAWC)*, pages 1–5.

[Alexandropoulos et al., 2021] Alexandropoulos, G. C., Shlezinger, N., Alamzadeh, I., Imani, M. F., Zhang, H., and Eldar, Y. C. (2021). Hybrid reconfigurable intelligent metasurfaces: Enabling simultaneous tunable reflections and sensing for 6G wireless communications. [Online] https://arxiv.org/abs/2104.04690.

[Alexandropoulos and Vlachos, 2020] Alexandropoulos, G. C. and Vlachos, E. (2020). A hardware architecture for reconfigurable intelligent surfaces with minimal active elements for explicit channel estimation. In *Proc. 2020 IEEE Int. Conf. Acoust. Speech Signal Process. (ICASSP)*, pages 9175–9179, Barcelona, Spain.

[Analog Devices, a] Analog Devices. GaAs pHEMT MMIC 2 Watt power amplifier, 27.3-33.5 GHz. *HMC906A datasheet*.

[Analog Devices, b] Analog Devices. Ka-band HPA. *HMC7054 datasheet*.

[Arslan et al., 2020] Arslan, E., Dogukan, A. T., and Basar, E. (2020). Index modulation-based flexible non-orthogonal multiple access. *IEEE Wireless Commun. Lett.*, 9(11):1942–1946.

[Arslan et al., 2022] Arslan, E., Yildirim, I., Kilinc, F., and Basar, E. (2022). Over-the-air equalization with reconfigurable intelligent surfaces. *IET Communications*, 16(13):1486–1497.

[Arzykulov et al., 2022] Arzykulov, S., Celik, A., Nauryzbayev, G., and Eltawil, A. M. (2022). UAV-assisted cooperative & cognitive NOMA: Deployment, clustering, and resource allocation. *IEEE Trans. Cogn. Commun.*, 8(1):263–281.

[Arzykulov et al., 2021] Arzykulov, S., Nauryzbayev, G., Celik, A., and Eltawil, A. M. (2021). Hardware and interference limited cooperative CR-NOMA networks under imperfect SIC and CSI. *IEEE Open J. Commun. Soc.*, 2:1473–1485.

[Balevi et al., 2018] Balevi, E., Rabee, F. T. A., and Gitlin, R. D. (2018). ALOHA-NOMA for massive machine-to-machine IoT communication. In *2018 IEEE Int. Conf. Commun. (ICC)*, pages 1–5.

[Basar, 2020] Basar, E. (2020). Reconfigurable intelligent surface-based index modulation: A new beyond MIMO paradigm for 6G. *IEEE Trans. Commun.*, 68(5):3187–3196.

[Basar, 2021] Basar, E. (2021). Reconfigurable intelligent surfaces for Doppler effect and multipath fading mitigation. *Front. Commun. Netw.*, 2:14.

[Basar et al., 2019] Basar, E., Di Renzo, M., De Rosny, J., Debbah, M., Alouini, M.-S., and Zhang, R. (2019). Wireless communications through reconfigurable intelligent surfaces. *IEEE Access*, 7:116753–116773.

[Basar and Poor, 2021] Basar, E. and Poor, H. V. (2021). Present and future of reconfigurable intelligent surface-empowered communications. *IEEE Signal Proc. Mag.*, 38(6):146–152.

[Basar and Yildirim, 2020] Basar, E. and Yildirim, I. (2020). SimRIS channel simulator for reconfigurable intelligent surface-empowered communication systems. In *Proc. IEEE Latin-Amer. Conf. Commun. (LATINCOM)*, pages 1–6.

[Basar et al., 2021] Basar, E., Yildirim, I., and Kilinc, F. (2021). Indoor and outdoor physical channel modeling and efficient positioning for reconfigurable intelligent surfaces in mmWave bands. *IEEE Trans. Commun.*, 69(12):8600–8611.

[Calvanese Strinati et al., 2021a] Calvanese Strinati, E., Alexandropoulos, G. C., et al. (2021a). Wireless environment as a service enabled by reconfigurable intelligent surfaces: The RISE-6G perspective. In *Proc. Joint EuCNC & 6G Summit*, pages 562–567.

[Calvanese Strinati et al., 2021b] Calvanese Strinati, E., Alexandropoulos, G. C., Wymeersch, H., Denis, B., Sciancalepore, V., D'Errico, R., Clemente, A., Phan-

Huy, D.-T., De Carvalho, E., and Popovski, P. (2021b). Reconfigurable, intelligent, and sustainable wireless environments for 6G smart connectivity. *IEEE Commun. Mag.*, 59(10):99–105.

[Celik, 2021] Celik, A. (2021). Grant-free NOMA: A low complexity power control through user clustering. [Online] http://dx.doi.org/10.36227/techrxiv.19688019.v1.

[Chen et al., 2022] Chen, J., Guo, L., Jia, J., Shang, J., and Wang, X. (2022). Resource allocation for IRS assisted SGF NOMA transmission: A MADRL approach. *IEEE J. Sel. Areas Commun.*, 40(4):1302–1316.

[Chen et al., 2021] Chen, Q., Li, M., Yang, X., Alturki, R., Alshehri, M. D., and Khan, F. (2021). Impact of residual hardware impairment on the IoT secrecy performance of RIS-assisted NOMA networks. *IEEE Access*, 9:42583–42592.

[C.Pan *et al.*, 2021] C.Pan *et al.* (2021). Reconfigurable intelligent surfaces for 6G systems: Principles, applications, and research directions. *IEEE Commun. Mag.*, 59(6):14–20.

[Di Renzo *et al.*, 2019] Di Renzo *et al.*, M. (2019). Smart radio environments empowered by reconfigurable AI meta-surfaces: An idea whose time has come. *EURASIP J. Wireless Commun. Netw.*, 129(1):1–20.

[Doğan et al., 2019] Doğan, S., Tusha, A., and Arslan, H. (2019). NOMA with index modulation for uplink URLLC through grant-free access. *IEEE J. Sel. Topics Signal Process.*, 13(6):1249–1257.

[Dunna et al., 2020] Dunna, M., Zhang, C., Sievenpiper, D., and Bharadia, D. (2020). ScatterMIMO: Enabling virtual MIMO with smart surfaces. In *Proc. 26th Annu. Int. Conf. Mobile Comput. Netw.*, pages 1–14.

[Elhattab et al., 2021] Elhattab, M., Arfaoui, M.-A., Assi, C., and Ghrayeb, A.

(2021). Reconfigurable intelligent surface assisted coordinated multipoint in downlink NOMA networks. *IEEE Commun. Lett.*, 25(2):632–636.

[Elkourdi et al., 2018] Elkourdi, M., Mazin, A., Balevi, E., and Gitlin, R. D. (2018). Enabling slotted aloha-NOMA for massive m2m communication in IoT networks. In *IEEE 19th Wireless Microw. Technol. Conf. (WAMICON)*, pages 1–4.

[Fayaz et al., 2021] Fayaz, M., Yi, W., Liu, Y., and Nallanathan, A. (2021). Transmit power pool design for grant-free NOMA-IoT networks via deep reinforcement learning. *IEEE Trans. Wireless Commun.*, 20(11):7626–7641.

[Flueck and Holland, 1973] Flueck, J. A. and Holland, B. S. (Washington, DC, 1973). The moments and distribution of the ratio of two gamma variables. In *Proc. Social Sci. Section, Amer. Stat. Assoc.*

[Grant and Boyd, 2014] Grant, M. and Boyd, S. (2014). CVX: Matlab software for disciplined convex programming, version 2.1. `http://cvxr.com/cvx`.

[Hemanth et al., 2020] Hemanth, A., Umamaheswari, K., Pogaku, A. C., Do, D.-T., and Lee, B. M. (2020). Outage performance analysis of reconfigurable intelligent surfaces-aided NOMA under presence of hardware impairment. *IEEE Access*, 8:212156–212165.

[Hou et al., 2020a] Hou, T., Liu, Y., Song, Z., Sun, X., Chen, Y., and Hanzo, L. (2020a). Reconfigurable intelligent surface aided NOMA networks. *IEEE J. Sel. Areas Commun.*, 38(11):2575–2588.

[Hou et al., 2020b] Hou, T., Liu, Y., Song, Z., Sun, X., Chen, Y., and Hanzo, L. (2020b). Reconfigurable intelligent surface aided noma networks. *IEEE J. Sel. Areas Commun.*, 38(11):2575–2588.

[Huang et al., 2019] Huang, C., Zappone, A., Alexandropoulos, G. C., Debbah, M., and Yuen, C. (2019). Reconfigurable intelligent surfaces for energy efficiency in wireless communication. *IEEE Trans. Wireless Commun.*, 18(8):4157–4170.

[Islam et al., 2017] Islam, S. M. R., Avazov, N., Dobre, O. A., and Kwak, K.-s. (2017). Power-domain non-orthogonal multiple access (NOMA) in 5G systems: Potentials and challenges. *IEEE Commun. Surv.*, 19(2):721–742.

[Jia et al., 2021] Jia, S., Yuan, X., and Liang, Y.-C. (2021). Reconfigurable intelligent surfaces for energy efficiency in D2D communication network. *IEEE Wireless Commun. Lett.*, 10(3):683–687.

[Jian et al., 2022] Jian, M., Alexandropoulos, G. C., Basar, E., Huang, C., Liu, R., Liu, Y., and Yuen, C. (to appear, 2022.). Reconfigurable intelligent surfaces for wireless communications: Overview of hardware designs, channel models, and estimation techniques. *ITU Intell. Converged Netw.* [Online] https://arxiv.org/abs/2203.03176.

[Joarder, 2009] Joarder, A. H. (2009). Moments of the product and ratio of two correlated chi-square variables. *Stat. Pap.*, 50(3):581–592.

[Khaleel and Basar, 2022] Khaleel, A. and Basar, E. (2022). A novel NOMA solution with RIS partitioning. *EEE J. Sel. Top. Signal Process.*, 16(1):70–81.

[Khaleel and Basar, 2021] Khaleel, A. and Basar, E. (to appear in 2021). A novel NOMA solution with RIS partitioning. *IEEE J. Sel. Areas Commun.*

[Kilinc et al., 2021] Kilinc, F., Yildirim, I., and Basar, E. (2021). Physical channel modeling for RIS-empowered wireless networks in sub-6 GHz bands. [Online] https://arxiv.org/abs/2111.01537.

[Lee et al., 1979] Lee, R.-Y., Holland, B. S., and Flueck, J. A. (1979). Distribution of a ratio of correlated gamma random variables. *SIAM J. Appl. Math.*, 36(2):304–320.

[Lin et al., 2021] Lin, S., Zheng, B., Alexandropoulos, G. C., Wen, M., Di Renzo, M., and Chen, F. (2021). Reconfigurable intelligent surfaces with reflection pat-

tern modulation: Beamforming design, channel estimation, and achievable rate analysis. *IEEE Trans. Wireless Commun.*, 20(2):741–754.

[Liu et al., 2021a] Liu, J., Wu, G., Zhang, X., Fang, S., and Li, S. (2021a). Modeling, analysis, and optimization of grant-free NOMA in massive MTC via stochastic geometry. *IEEE Internet Things J.*, 8(6):4389–4402.

[Liu et al., 2021b] Liu, X., Liu, Y., Chen, Y., and Poor, H. V. (2021b). RIS enhanced massive non-orthogonal multiple access networks: Deployment and passive beamforming design. *IEEE J. Sel. Areas Commun.*, 39(4):1057–1071.

[Liu et al., 2022] Liu, Y., Mu, X., Liu, X., Di Renzo, M., Ding, Z., and Schober, R. (2022). Reconfigurable intelligent surface-aided multi-user networks: Interplay between NOMA and RIS. *IEEE Wireless Commun.*, 29(2):169–176.

[Long et al., 2021] Long, R., Liang, Y.-C., Pei, Y., and Larsson, E. G. (2021). Active reconfigurable intelligent surface-aided wireless communications. *IEEE Trans. Wireless Commun.*, 20(8):4962–4975.

[Makki et al., 2015a] Makki, B., Svensson, T., Eriksson, T., and Nasiri-Kenari, M. (2015a). On the throughput and outage probability of multi-relay networks with imperfect power amplifiers. *IEEE Trans. Wireless Commun.*, 14(9):4994–5008.

[Makki et al., 2015b] Makki, B., Svensson, T., Eriksson, T., and Nasiri-Kenari, M. (2015b). On the throughput and outage probability of multi-relay networks with imperfect power amplifiers. *IEEE Trans. Wireless Commun.*, 14(9):4994–5008.

[Nguyen et al., 2021] Nguyen, N. T., Vu, Q.-D., Lee, K., and Juntti, M. (2021). Hybrid relay-reflecting intelligent surface-assisted wireless communication. [Online] https://arxiv.org/abs/2103.03900.

[Pattipati et al., 1992] Pattipati, K., Deb, S., Bar-Shalom, Y., and Washburn, R. (1992). A new relaxation algorithm and passive sensor data association. *IEEE Trans. Autom. Control*, 37(2):198–213.

[Persson et al., 2013] Persson, D., Eriksson, T., and Larsson, E. G. (2013). Amplifier-aware multiple-input multiple-output power allocation. *IEEE Commun. Lett.*, 17(6):1112–1115.

[Provost and Rudiuk, 1994] Provost, S. B. and Rudiuk, E. M. (1994). The exact density function of the ratio of two dependent linear combinations of chi-square variables. *Ann. Inst. Stat. Math.*, 46(3):557–571.

[Saad et al., 2020] Saad, W., Bennis, M., and Chen, M. (2020). A vision of 6G wireless systems: Applications, trends, technologies, and open research problems. *IEEE Netw.*, 34(3):134–142.

[Saito et al., 2013] Saito, Y., Kishiyama, Y., Benjebbour, A., Nakamura, T., Li, A., and Higuchi, K. (2013). Non-orthogonal multiple access (NOMA) for cellular future radio access. In *2013 IEEE 77th Veh. Technol. Conf.*, pages 1–5.

[Sarkar et al., 2017] Sarkar, A., Aryanfar, F., and Floyd, B. A. (2017). A 28-GHz SiGe BiCMOS PA with 32% efficiency and 23-dBm output power. *IEEE J. Solid-State Circuits*, 52(6):1680–1686.

[Shahab et al., 2020] Shahab, M. B., Abbas, R., Shirvanimoghaddam, M., and Johnson, S. J. (2020). Grant-free non-orthogonal multiple access for IoT: A survey. *IEEE Commun. Surv. Tutor.*, 22(3):1805–1838.

[Shlezinger et al., 2021] Shlezinger, N., Alexandropoulos, G. C., Imani, M. F., Eldar, Y. C., and Smith, D. R. (2021). Dynamic metasurface antennas for 6G extreme massive MIMO communications. *IEEE Wireless Commun.*, 28(2):106–113.

[Tang et al., 2021] Tang, Z., Hou, T., Liu, Y., Zhang, J., and Zhong, C. (2021). A novel design of RIS for enhancing the physical layer security for RIS-aided NOMA networks. *IEEE Wireless Commun. Lett.*, 10(11):2398–2401.

[Uysal, 2009] Uysal, M. (2009). *Cooperative Communications for Improved Wireless Network Transmission: Framework for Virtual Antenna Array Applications*. IGI-Global, Hershey, PA, USA.

[Wu and Zhang, 2019] Wu, Q. and Zhang, R. (2019). Intelligent reflecting surface enhanced wireless network via joint active and passive beamforming. *IEEE Trans. on Wireless Commun.*, 18(11):5394–5409.

[Wu and Zhang, 2020] Wu, Q. and Zhang, R. (2020). Towards smart and reconfigurable environment: Intelligent reflecting surface aided wireless network. *IEEE Commun. Mag.*, 58(1):106–112.

[Wu et al., 2021] Wu, Q., Zhang, S., Zheng, B., You, C., and Zhang, R. (2021). Intelligent reflecting surface-aided wireless communications: A tutorial. *IEEE Trans. Commun.*, 69(5):3313–3351.

[Yang et al., 2021a] Yang, G., Xu, X., Liang, Y.-C., and Renzo, M. D. (2021a). Reconfigurable intelligent surface-assisted non-orthogonal multiple access. *IEEE Trans. Wireless Commun.*, 20(5):3137–3151.

[Yang et al., 2021b] Yang, Z., Liu, Y., Chen, Y., and Al-Dhahir, N. (2021b). Machine learning for user partitioning and phase shifters design in RIS-aided NOMA networks. *IEEE Trans. Commun.*, 69(11):7414–7428.

[Yildirim et al., 2021a] Yildirim, I., Kilinc, F., Basar, E., and Alexandropoulos, G. C. (2021a). Hybrid RIS-empowered reflection and decode-and-forward relaying for coverage extension. *IEEE Commun. Lett.*, 25(5):1692–1696.

[Yildirim et al., 2021b] Yildirim, I., Uyrus, A., and Basar, E. (2021b). Modeling and analysis of reconfigurable intelligent surfaces for indoor and outdoor applications in future wireless networks. *IEEE Trans. Commun.*, 69(2):1290–1301.

[Yuan et al., 2021] Yuan, J., Wen, M., Li, Q., Basar, E., Alexandropoulos, G. C., and Chen, G. (2021). Receive quadrature reflecting modulation for RIS-

empowered wireless communications. *IEEE Trans. Veh. Technol.*, 70(5):5121–5125.

[Zhang et al., 2022] Zhang, C., Liu, Y., and Ding, Z. (2022). Semi-grant-free NOMA: A stochastic geometry model. *IEEE Trans. Wireless Commun.*, 21(2):1197–1213.

[Zhang et al., 2020] Zhang, C., Qin, Z., Liu, Y., and Chai, K. K. (2020). Semi-grant-free uplink NOMA with contention control: A stochastic geometry model. In *2020 IEEE Int. Conf. Commun. (ICC) Workshops (ICC Workshops)*, pages 1–6.

[Zhang et al., 2021] Zhang, Z., Zhang, C., Jiang, C., Jia, F., Ge, J., and Gong, F. (2021). Improving physical layer security for reconfigurable intelligent surface aided NOMA 6G networks. *IEEE Trans. Veh. Tech.*, 70(5):4451–4463.

[Zhang *et al.*, 2021] Zhang *et al.*, Z. (2021). Active RIS vs. passive RIS: which will prevail in 6G? [Online] https://arxiv.org/abs/2103.15154.

[Zhong et al., 2022] Zhong, R., Liu, Y., Mu, X., Chen, Y., and Song, L. (2022). AI empowered RIS-assisted NOMA networks: Deep learning or reinforcement learning? *IEEE J. Sel. Areas Commun.*, 40(1):182–196.

[Zuo et al., 2020] Zuo, J., Liu, Y., Basar, E., and Dobre, O. A. (2020). Intelligent reflecting surface enhanced millimeter-wave NOMA systems. *IEEE Commun. Lett.*, 24(11):2632–2636.

Appendix A

Table A.1: The shape (k) and scale (ν) parameters of the fitted Gamma distribution

P_{max}(dBm)	N	P_t (dBm) :	-10	-5	0	5	10	15	20	25	30
10	64	k	44.8922	44.7180	44.7905	44.7109	44.8358	44.8963	48.0934	58.6428	58.7049
		ν	0.000405	0.001287	0.004063	0.012868	0.040595	0.128166	0.375257	0.329909	0.329483
	256	k	178.8281	178.8481	179.1008	178.2996	233.7027	234.8395	234.5761	233.9432	234.3112
		ν	0.006486	0.020508	0.064762	0.205720	0.330019	0.328426	0.328834	0.329725	0.329212
20	64	k	44.8284	44.7199	44.7593	44.84389	44.8633	44.7232	44.7599	44.7586	47.9274
		ν	0.000406	0.001286	0.004066	0.012835	0.040551	0.128680	0.406483	1.285651	3.765564
	256	k	178.2811	178.9068	178.4629	178.8242	178.8931	178.6688	234.2556	234.8709	233.5700
		ν	0.006505	0.020503	0.064994	0.205099	0.648377	2.052960	3.292076	3.283723	3.302386